Dynamic evolution of porosity in lower-crustal faults during the earthquake cycle

JGR Solid Earth

RESEARCH ARTICLE
10.1029/2023JB026809

Dynamic Evolution of Porosity in Lower-Crustal Faults During the Earthquake Cycle

Stephen Paul Michalchuk[1], Sascha Zertani[1], François Renard[1,2], Florian Fusseis[3], Alireza Chogani[4], Oliver Plümper[4], and Luca Menegon[1]

[1]The Njord Centre, Departments of Geosciences and Physics, University of Oslo, Oslo, Norway, [2]Isterre, Université Grenoble Alpes, Université Savoie Mont Blanc, CNRS, IRD, Université Gustave Eiffel, Grenoble, France, [3]School of Geosciences, Grant Institute, The University of Edinburgh, Edinburgh, UK, [4]Department of Earth Sciences, Utrecht University, Utrecht, the Netherlands

Key Points:

- Fracture porosity is healed in the wall rock, while porosity from metamorphic recrystallization is preserved in the pseudotachylyte vein
- Porosity in the pseudotachylyte is poorly interconnected and is concentrated around garnets and in survivor clasts from the wall rock
- Porosity in the mylonite is greatly reduced because of precipitation of phases in transient pores during grain-size sensitive creep

Supporting Information:

Supporting Information may be found in the online version of this article.

Correspondence to:

S. P. Michalchuk,
stephen.michalchuk@geo.uio.no

Citation:

Michalchuk, S. P., Zertani, S., Renard, F., Fusseis, F., Chogani, A., Plümper, O., & Menegon, L. (2023). Dynamic evolution of porosity in lower-crustal faults during the earthquake cycle. *Journal of Geophysical Research: Solid Earth*, *128*, e2023JB026809. https://doi.org/10.1029/2023JB026809

Received 28 MAR 2023
Accepted 26 JUL 2023

Author Contributions:

Conceptualization: Luca Menegon
Data curation: Stephen Paul Michalchuk
Formal analysis: Stephen Paul Michalchuk, Sascha Zertani, Luca Menegon
Funding acquisition: Luca Menegon
Investigation: Stephen Paul Michalchuk, Alireza Chogani
Methodology: Luca Menegon
Resources: Luca Menegon
Software: Sascha Zertani
Supervision: Luca Menegon
Validation: Stephen Paul Michalchuk
Visualization: Stephen Paul Michalchuk

Abstract Earthquake-induced fracturing of the dry and strong lower crust can transiently increase permeability for fluids to flow and trigger metamorphic and rheological transformations. However, little is known about the porosity that facilitates these transformations. We analyzed microstructures that have recorded the mechanisms generating porosity in the lower crust from a pristine pseudotachylyte (solidified earthquake-derived frictional melt) and a mylonitized pseudotachylyte from Lofoten, Norway to understand the evolution of fluid pathways from the coseismic to the post- and interseismic stages of the earthquake cycle. Porosity is dispersed and poorly interconnected within the pseudotachylyte vein (0.14 vol%), with a noticeably increased amount along garnet grain boundaries (0.25–0.41 vol%). This porosity formed due to a net negative volume change at the grain boundary when garnet overgrows the pseudotachylyte matrix. Efficient healing of the damage zone by fluid-assisted growth of feldspar neoblasts resulted in the preservation of only a few but relatively large interconnected pores along coseismic fractures (0.03 vol% porosity). In contrast, porosity in the mylonitized pseudotachylyte is dramatically reduced (0.02 vol% overall), because of the efficient precipitation of phases (amphibole, biotite and feldspars) into transient pores during grain-size sensitive creep. Porosity reduction on the order of >85% may be a contributing factor in shear zone hardening, potentially leading to the development of new pseudotachylytes overprinting the mylonites. Our results show that earthquake-induced rheological weakening of the lower crust is intermittent and occurs when a fluid can infiltrate a transiently permeable shear zone, thereby facilitating diffusive mass transfer and creep.

Plain Language Summary Earthquakes create fractures and increase the porosity in crustal rocks. These fractures can help transport fluids to newly accessible regions in the crust, which in turn may kickstart metamorphic reactions, and potentially alter the rheology. However, very little is known about the mechanisms, the microstructural context, and the morphology of this increased porosity. We analyzed ancient earthquake-generated frictional melts (pseudotachylytes) and their immediate damage zone in the host rock, as well as plasticly deformed pseudotachylytes, that have since been exhumed from depth and are now exposed at the surface in Lofoten, Norway. We analyzed these rocks to determine the processes that create porosity and how this porosity evolves with increasing plastic deformation. The pseudotachylyte hosts more porosity than the damage zone immediately flanking the vein, in particular there is a high concentration of porosity around garnets. We interpret this porosity to have formed as a result of the metamorphic growth of garnet. Much of the fracture-related porosity created during the initial earthquake has been efficiently sealed. Porosity is greatly reduced in the sheared pseudotachylytes because of solution-precipitation processes that operated during ductile deformation. Porosity reduction may reflect fluid consumption, leading to shear zone hardening and possibly new pseudotachylyte formation.

1. Introduction

Earthquakes are key agents of metamorphic and structural transformations of the lower crust. Lower-crustal earthquakes induce modifications of the mineralogy, density, and rheology of the rocks (Jamtveit et al., 2019) that have direct effects on the lithospheric response to major geodynamic processes, including continental collision (Copley et al., 2011; Craig et al., 2012) and rifting (Craig et al., 2011), and on the stability of deep mountain roots (Jackson et al., 2004). Such transformations of the lower crust are dependent on the availability of externally derived or locally produced (e.g., by dehydration reactions) aqueous fluids (Jamtveit et al., 2016; Putnis

Writing – original draft: Stephen Paul Michalchuk
Writing – review & editing: Sascha Zertani, François Renard, Florian Fusseis, Oliver Plümper, Luca Menegon

et al., 2017). Thus, in the absence of fluids, the lower crust will not undergo metamorphic and rheological transformations and will remain dry, impermeable, metastable, and mechanically strong (Jamtveit et al., 2019; Yardley & Valley, 1997).

In crystalline rocks at lower-crustal depths, the confining pressure is on the order of gigapascals and very little porosity (~0.1%) is available to facilitate fluid flow (Thompson & Connolly, 1990). Earthquakes causing fragmentation, wall-rock damage, and seismic slip have been identified as the most effective processes for creating permeable fracture networks and transiently permitting the introduction of fluids into a metastable host rock that will react and metamorphose into a transiently mechanically weaker lithology (Austrheim, 1987; Jamtveit et al., 2016; Jolivet et al., 2005; Kaatz et al., 2021; Zertani et al., 2019).

Pseudotachylytes, solidified frictional melt produced during seismic slip, have been studied in detail from several localities to gain insights into earthquake nucleation and coseismic processes in the lower crust (Campbell et al., 2020; Dunkel et al., 2021; Hawemann et al., 2018; Orlandini & Mahan, 2020; Petley-Ragan et al., 2019). Recent studies have demonstrated that microstructures of lower-crustal pseudotachylytes can preserve a time-lapse record of the coseismic processes during a single earthquake followed by post- and interseismic healing and creep (Campbell & Menegon, 2022; Mancktelow et al., 2022; Petley-Ragan et al., 2021). Coseismic processes preserved in the microstructure include the rupture propagation with the associated off-fault damage, frictional heating and melting during fault slip, followed by rapid solidification (quenching) and crystallization of new minerals. Post- and interseismic healing and creep manifest themselves as (a) fracture sealing in the damage zone, typically in the form of precipitation of secondary minerals from the infiltrating fluids (Petley-Ragan et al., 2019), and (b) mylonitization (solid-state viscous creep) of pseudotachylytes facilitated by fluid infiltration and weakening along faults initially characterized by frictional melting and wall-rock damage (Menegon et al., 2017). Although the microstructures signifying fracture-induced fluid pathways and infiltration of fluids promoting metamorphic and rheological changes have been well-documented (Austrheim, 1987), the evolution of this associated porosity as the coseismic pseudotachylyte becomes mylonitized in the post- and interseismic stages needs to be characterized.

Thus far, porosity has been characterized to control fault strength in upper-crustal cataclasites and fault gouge (Kirilova et al., 2020), or to be related to melt degassing during coseismic slip in fluid-rich upper-crustal pseudotachylytes (Boullier et al., 2001; Gomila et al., 2021; Magloughlin, 2011; Rowe et al., 2005). In this contribution we report a detailed microstructural account of porosity in pristine and mylonitized pseudotachylytes from the lower-crustal anorthosites of Lofoten, Norway. Our aim is to understand the porosity generating mechanisms and characterize the fluid pathways using synchrotron X-ray microtomography (SμCT), focused-ion-beam scanning electron microscopy (FIB-SEM) nanotomography, SEM-cathodoluminescence (SEM-CL), and electron backscatter diffraction (EBSD) to reveal the dynamic evolution of porosity during the earthquake cycle.

2. Geological Setting

The Lofoten Archipelago in northern Norway is a NNE-SSW trending basement horst that exposes a window into a lower-crustal section of the Baltica plate consisting of Archean to Paleoproterozoic ortho- and paragneisses, that were intruded by a large Anorthosite-Mangerite-Charnockite-Granite (AMCG) suite between 1.9 and 1.7 Ga (Corfu, 2004). The anhydrous AMCG suite emplaced into granulitic crust at ambient conditions of ~750–800°C and 0.4–1.2 GPa (Markl et al., 1998). The primary igneous fabrics and the granulite-facies mineral assemblage are generally well preserved.

These anhydrous granulites largely escaped the Caledonian tectono-metamorphic overprint due to a limited supply of fluids necessary to facilitate viscous deformation (Steltenpohl et al., 2004). Where there is deformation, Caledonian-aged fabrics and structures are limited to localized shear zones that developed under granulite-, eclogite-, and/or upper amphibolite-facies conditions (Kullerud et al., 2001; Menegon et al., 2013; Steltenpohl et al., 2004, 2011). Fracturing and the formation of pseudotachylytes are reported to be the essential precursor processes for shear zone initiation (Menegon et al., 2013, 2017; Steltenpohl et al., 2006).

Exposed on the eastern ridge flanking the Nusfjord on Flakstadøy, is a kilometer-scale outcrop of coarse-grained anorthosite consisting of gray to dark purple plagioclase (crystals as large as 20 cm) and a subordinate (<10%) amount of clinopyroxene, orthopyroxene, olivine, and iron-titanium oxides. The anorthosite hosts mutually overprinting pseudotachylytes and mylonitized pseudotachylytes within the Nusfjord East shear zone network

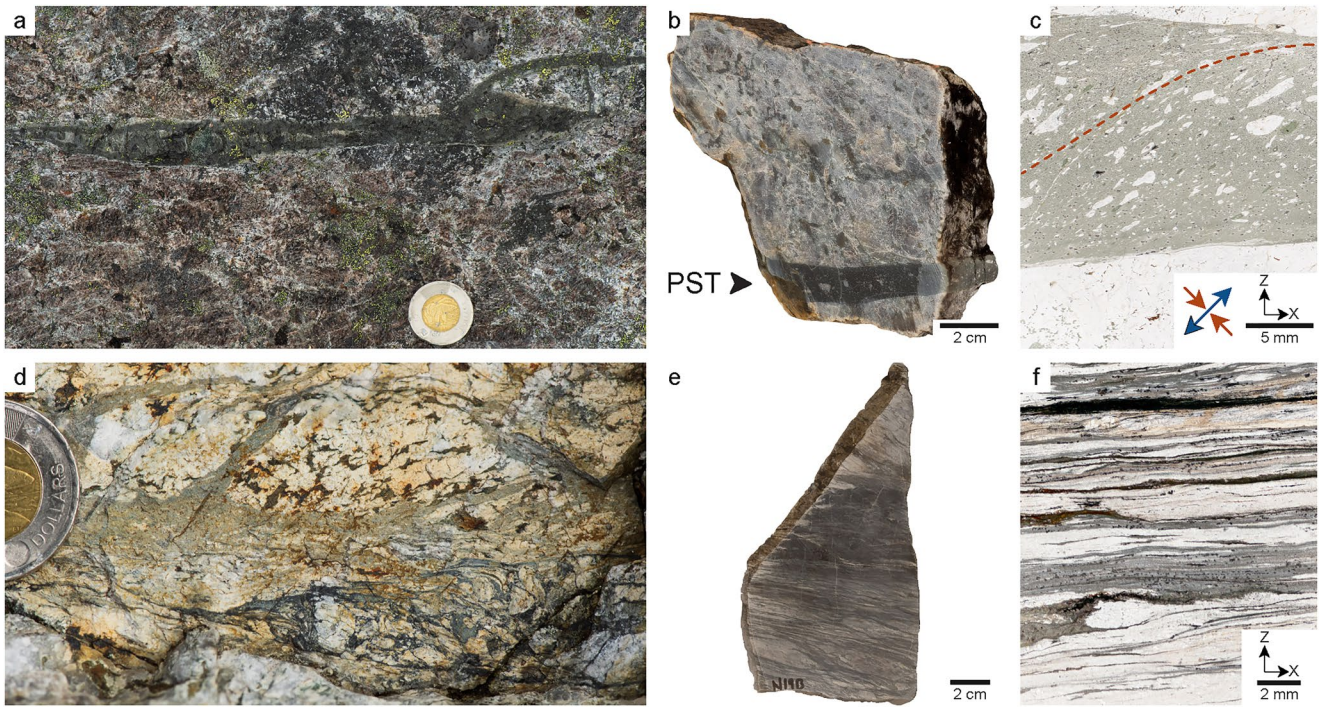

Figure 1. (a) Field image of a pristine pseudotachylyte with an injection vein protruding from the main slip surface into the host anorthosite. (b and c) Hand sample and thin section of the pristine pseudotachylyte LM1726 (pseudotachylyte indicated with PST) The dashed brown line in (c) highlights a weak internal foliation, in addition to the incremental extension direction (blue arrows) and the incremental shortening direction (brown arrows). (d) Field image of the ductile shear zone from which the mylonitized pseudotachylyte N19 was sampled. Light and dark green material represent two different generations of pseudotachylyte breccia that experienced ductile deformation. Relict structures from the original pseudotachylytes include injection veins and angular survivor clasts of host rock plagioclase, however they display some amount of stretching, elongating, flattening, and rotation due to ductile deformation. (e and f) Hand sample and thin section of the mylonitized pseudotachylyte N19. Canadian two-dollar coin (28 mm) for scale in field images.

(Campbell et al., 2020; Menegon et al., 2017). The network consists of three main intersecting sets of ductile shear zones ranging in width from 1 cm to 1 m, with all three sets containing mylonitized pseudotachylytes (type-1 pseudotachylytes defined by Campbell et al. (2020); Figure 1d). The three ductile shear zone sets form boundaries around relatively undeformed anorthosite blocks that contain pristine (non-mylonitized) pseudotachylytes (type-2 pseudotachylytes defined by Campbell et al. (2020); Figure 1a). Field relationships demonstrate that type-2 pseudotachylytes formed during ongoing viscous creep of the type-1 pseudotachylytes (Campbell et al., 2020). The formation and mylonitization of pseudotachylytes occurred under lower-crustal conditions of 650–750°C and 0.7–0.9 GPa. About 0.20–0.40 wt. % H_2O infiltrated the fault zones and accompanied the mylonitization of pseudotachylytes. The infiltrated H_2O was redistributed along the grain boundaries in the pseudotachylyte and in the fractured domains (Menegon et al., 2017).

3. Materials and Methods

3.1. Microstructural Observations and Electron Backscatter Diffraction (EBSD)

Two samples were investigated in this study: a type-2 pristine pseudotachylyte vein LM1726 (UTM WGS84: 33W 432142E; 7549923N; Figure 1b), and a type-1 mylonitized pseudotachylyte N19 (UTM WGS84: 33W 432042E; 7549520N; Figure 1e). The pseudotachylyte vein LM1726 is subvertical and trends NE-SW. It cuts a pegmatite dyke with an apparent offset of ~7 cm. Therefore, LM1726 is a fault vein and not an injection vein. The mylonitized pseudotachylyte (sample N19, Figures 1d and 1e) was collected from a ductile shear zone first described by Menegon et al. (2017) and interpreted as a composite banding of multiple generations of mutually overprinting pseudotachylytes and mylonites reflecting the cyclic interplay between brittle and viscous deformation at lower-crustal condition. N19 dips 58° toward 146°, and has a stretching lineation plunging 46° toward 190°. The kinematics are oblique-normal.

Compositional variations between the pristine- and mylonitized pseudotachylytes and their anorthosite host rock in Nusfjord are limited (Jamtveit et al., 2019; Menegon et al., 2017). The most notable change consists in a

six to tenfold increase in aqueous fluid content necessary to stabilize the amphibole-bearing mineral assemblage in the mylonitized pseudotachylytes compared to the anhydrous anorthosite (i.e., ≥0.25 wt. % of H_2O vs. 0.04 wt.%, Menegon et al., 2017). The present paper investigates the porosity network in the pristine- and mylonitized pseudotachylytes that facilitated fluid infiltration.

Thin sections (Figures 1c and 1f) were analyzed using polarized light microscopy and scanning electron microscopy (SEM) coupled with cathodoluminescence (SEM-CL). Observations were made on polished thin sections cut perpendicular to the foliation and parallel to the stretching lineation (sample N19), and perpendicular to the pseudotachylyte vein boundary (sample LM1726). SEM and SEM-CL analyses were performed at the Goldschmidt Laboratory, Department of Geosciences, University of Oslo using a Hitachi SU5000 FEG-SEM coupled with a Delmic Sparc Advanced CL system. To reduce vignetting along the margins of individual images of the tiled mosaic, CL maps were acquired at 500X magnification, using an accelerating voltage of 15 kV, a 25 ms dwell time, a 0.04 ms exposure time, and a 10%–15% image overlap.

Major element compositions were spot analyzed by wavelength-dispersive spectrometry with a Cameca SX100 election microprobe analyzer (EMPA; Department of Geosciences, University of Oslo), using an accelerating voltage of 15 kV, beam currents between 10 and 20 nA, and a 1 μm beam diameter. Feldspar and garnet point analyses are presented in compositional diagrams using MinPlot (Walters, 2022). X-ray intensity maps were acquired using an accelerating voltage of 15 kV, 40 nA accelerating voltage, 400 ms dwell time, and a step size of 1 μm. Nine elements (Si, Al, Fe, Mn, Mg, Na, Ca, K, and Ba) were measured at the specific wavelength in two passes. X-ray maps were classified and standardized using XMapTools (Lanari et al., 2014). Compositional mapping followed the procedure of Lanari et al. (2019) whereby X-ray intensity maps were standardized using spot analyses as internal standards within XMapTools 4 (beta 2) build version 220512. Furthermore, spot analyses of representative compositions for garnet rims, plagioclase, and amphibole grains were used to calculate mineral densities at lower-crustal conditions in Thermolab v22_03_23 (Vrijmoed & Podladchikov, 2022).

Crystallographic orientation of sample N19 were collected via EBSD analysis using a Zeiss Merlin SEM coupled with an Oxford Instruments Nordlys S detector at the University of Tromsø. EBSD data were collected after SEM-CL on the same representative microstructures. All thin sections were chemically polished with colloidal silica prior to EBSD analysis. Crystallographic patterns were acquired and processed using Aztec software (Oxford Instruments) on rectangular grids with a step size of 1 μm using an accelerating voltage of 20 kV, a 70° sample title angle, and a 24–29 mm working distance. EBSD results for plagioclase are presented as phase maps, pole figures, and misorientation angle distribution histograms. Pole figures are orientated with their horizontal diameter corresponding to the trace of the mylonitic foliation (E-W) and parallel to the stretching lineation.

3.2. Synchrotron X-Ray Microtomography (SμCT)

In order to document the porosity and mineral phase distributions, we scanned cylindrical subsamples from LM1726 and N19 in four μCT data sets each at the TOMCAT beamline X02DA of the Swiss Light Source at the Paul Scherrer Institute in Switzerland. The cylinders (~5 mm height and 2 mm diameter) were drilled perpendicular or near-perpendicular to the foliation and to the pseudotachylyte vein boundary. Two N19 volumes acquired at 10X magnification and two acquired at 20X magnification. All four LM1726 volumes were acquired at 10X magnification. The samples were imaged with a monochromatic beam energy of 28 keV. A charge-couple device camera collected images at 0.1° angular steps over 180° for a total of 1,801 projections with dimensions of 2,560 × 2,160 pixels. 3D volumes with dimensions of 2,560 × 2,560 × 2,160 voxels were reconstructed from these projections using a direct Fourier method and an efficient data reconstruction pipeline (Marone et al., 2017). Data was corrected to reduce ring-artifacts. The voxel size of the reconstructed data is 0.65^3 μm³ (10X magnification) and 0.325^3 μm³ (20X magnification), respectively. Resolution is twice the value of the voxel size. The data sets were processed, segmented, analyzed and visualized in Avizo (Thermo Fischer Scientific). Depending on the noise filtering algorithm, the segmentation method, and the interconnectivity options between voxels employed, final porosity values can vary (see Kirilova et al., 2020; McBeck et al., 2021 and references therein). All SμCT volumes were processed similarly with the same workflow recipe. This study is foremost interested in trends of the porosity distribution, with less focus on the absolute values. See Text S1 in Supporting Information S1 for further details on segmentation procedures.

Pores in direct contact with the garnet grain boundary are used in the porosity measurements regarding garnet, while pores encapsulated within the survivor clasts are considered in the survivor clast measurements.

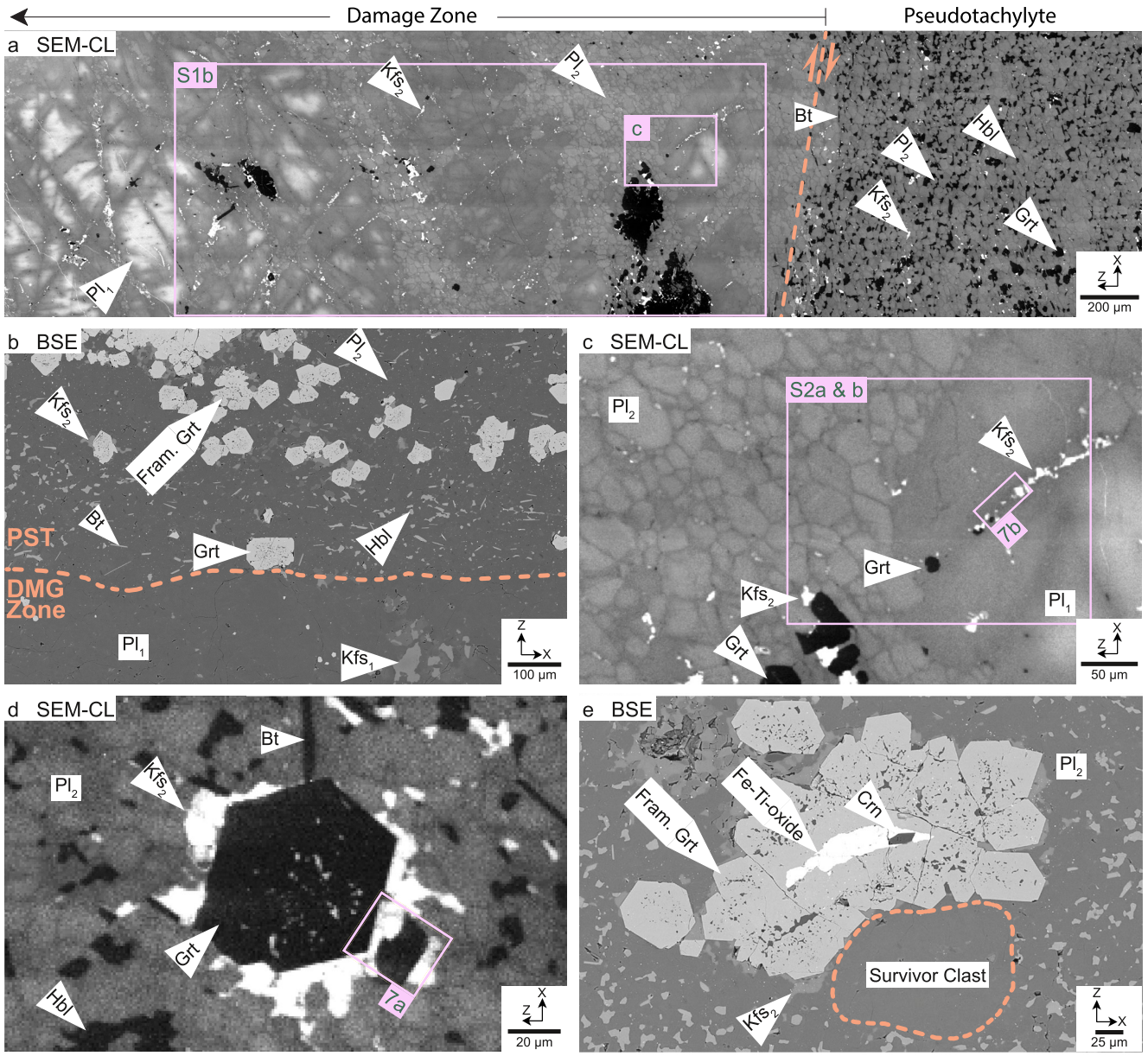

Figure 2. Representative microstructures in LM1726. (a) SEM-CL mosaic map of the pseudotachylyte vein margin and the immediate damage zone in the host anorthosite. The anorthosite crystals are variably fractured with minimal offset into angular fragments with variable CL intensity zonation from bright gray cores to darker gray rims. Black grains in CL are denser phases such as garnet, amphibole, pyroxene, and biotite. Equant plagioclase$_2$ neoblasts grains (<20 µm diameter) nucleated from the smallest fragments of anorthosite are medium gray CL intensity. The white <10 µm grains are K-feldspar$_2$ grains enriched in BaO. (b) backscatter electron (BSE) image of the pseudotachylyte vein (PST) margin with the damage zone (DMG Zone). Garnet appears as both single grains (Grt) and framboidal forms (Fram. Grt). There is a marked increase in biotite along the vein margin. See Figure S1a in Supporting Information S1 for a larger version. (c) Magnified SEM-CL from (a) of a plagioclase$_1$ fragment with a bright CL core, and progressively darker CL toward the rim. A crack within the plagioclase$_1$ fragment has been efficiently healed with K-feldspar$_2$ and was further analyzed with focused-ion-beam scanning electron microscopy (FIB-SEM) nanotomography in Figure 7b. Plagioclase EMPA maps are provided in Figures S2a and S2b of the Supporting Information S1. (d) SEM-CL of a single garnet grain inside the pseudotachylyte vein with associated microstructures. Barium-enriched K-feldspar has formed asymmetrical rims around the garnet and has a bright CL intensity. Pink rectangle indicates a FIB-SEM nanotomography transect (Figure 7a). (e) BSE of a framboidal garnet (Fram. Grt) inside the pseudotachylyte vein with a core consisting of an Fe-Ti-oxide and corundum, with smaller quartz and amphibole inclusions in the mantle region.

3.3. Focused Ion Beam Scanning Electron Microscopy (FIB-SEM)

Two locations in LM1726 were analyzed with FIB-assisted nanotomography to determine healing mechanisms in the damage zone (Site 1; see Figure 2c) and porosity generating mechanisms around garnet in the pseudotachylyte

matrix (Site 2; see Figure 2d). The analysis was conducted on an FEI Helios NanoLab G3 UC at Utrecht University using an accelerating voltage of 5 kV, a beam current of 0.10 nA, a working distance of 4.1 mm, and a tilt angle of 52°. A 3 μs dwell time was used to acquire each backscatter electron (BSE) image of every slice and a tilt correction was applied to each image at the time of acquisition. Slice interval was every 100 nm for both locations, with Site 1 having a pixel dimension of 4.9×6.2 nm^2 and Site 2 having a pixel dimension of 4.5×5.7 nm^2. Images were then segmented using Ilastik (Berg et al., 2019) and visualized with Avizo software. Segmented volumes have a "stepped" appearance because of the 100 nm between slices that prevented Avizo from interpolating the distance between.

4. Results

4.1. Microstructures and Mineral Chemistry

4.1.1. Pristine Pseudotachylyte and Its Damage Zone

Primary (magmatic) plagioclase in the host anorthosite is denoted as plagioclase$_1$, while the plagioclase neoblasts that grew as a result of deformation are denoted as plagioclase$_2$. The same subscript notation is used for K-feldspar. Minerals in text and figures follow abbreviations from Whitney and Evans (2010).

The damage zone in the host anorthosite is the centimeter-scale zone immediately flanking the pseudotachylyte margin (Figures 2a and 2b; Figure S1a in Supporting Information S1). It consists of intensely fractured angular fragments of plagioclase$_1$, many of which display undulatory extinction and deformation twins (Figure S1b in Supporting Information S1). There is very little rotation and negligible offset along fractures. Fractures between plagioclase$_1$ fragments can be between a few microns to 200 μm wide and are filled predominately with plagioclase$_2$ neoblasts and a subordinate amount of K-feldspar$_2$ neoblasts (Figures 2a and 2c; Figure S1c in Supporting Information S1). The fractured plagioclase$_1$ grains display a core-to-rim CL intensity zonation from bright to dark gray (Figures 2a and 2c). Plagioclase$_2$ neoblasts are 10–30 μm sized, generally polygonal grains displaying uniform light gray CL intensity. K-feldspar$_2$ neoblasts are generally smaller (<15 μm), polygonal- to cuspate-shaped, and are found in triple junctions between plagioclase$_2$ grains, as well as in discontinuous arrays lining thin (≤10 μm wide) intracrystalline fractures (Figure 2c). K-feldspar$_2$ appears white under CL. Garnet in the damage zone commonly occurs as single euhedral grains <50 μm in size, free of inclusions, and occurs amongst the plagioclase$_2$ and K-feldspar$_2$ neoblasts in the plagioclase$_1$ intracrystalline cracks. Pyroxene is variably fractured and replaced by amphibole.

The 10–15 mm thick pseudotachylyte vein locally preserves primary quenching crystallization microstructures, such as radiating microlites of plagioclase$_2$, chilled margins, dendritic-framboidal garnet clusters, and flow structures (Figure 2b; Figures S1a and S1d in Supporting Information S1) that reflect rapid crystallization from a melt. The fine-grained (<25 μm) microcrystalline matrix is dominated by plagioclase$_2$ and amphibole, with a subordinate amount of garnet, K-feldspar$_2$, biotite, and scapolite. Survivor clasts are composed predominantly of angular to rounded polycrystalline aggregates of variably fractured plagioclase$_1$ grains from the host anorthosite (Figures S1a and S1d in Supporting Information S1). Fractures in the plagioclase$_1$ are filled by equant plagioclase$_2$ neoblasts (10–30 μm sized). Fractured plagioclase$_1$ grains display undulatory extinction, deformation twins, and under SEM-CL have a zoning with bright cores and dark gray rims, like in the damage zone (Figure S1e in Supporting Information S1). Garnets are euhedral and occur as single grains (<75 μm; Figure 2d) or as clusters of mutually intergrown euhedral grains having a framboidal appearance (100–120 μm; Figure 2e). Often the framboidal garnets are enclosing cores containing tens of micron-sized clinopyroxene (partially replaced by amphibole) or Fe-Ti oxides ±corundum. Garnets in the pseudotachylyte, both single grains and framboidal varieties, contain inclusion-rich cores consisting predominately of <10 μm quartz, clinopyroxene or amphibole, K-feldspar, and iron oxides, while their rims are free of inclusions. Garnets are usually wrapped by a bright CL intensity, locally asymmetrical, rim (5–10 μm wide) of K-feldspar$_2$ (Figure 2d; Figure S1e in Supporting Information S1). Neoblasts of K-feldspar$_2$ also occur as fine (<5 μm) isolated grains in the pseudotachylyte matrix. Although the pseudotachylyte vein largely preserves primary microstructures as described above, a slight solid-state shear overprint is evident on one side of the pseudotachylyte vein in the form of slightly elongate and aligned survivor clasts defining a weak internal foliation. Where asymmetrical, the rims of K-feldspar around garnet are aligned parallel to the incremental extension direction associated with the solid-state overprint (Figures 1c and 2d; Figure S1e in Supporting Information S1).

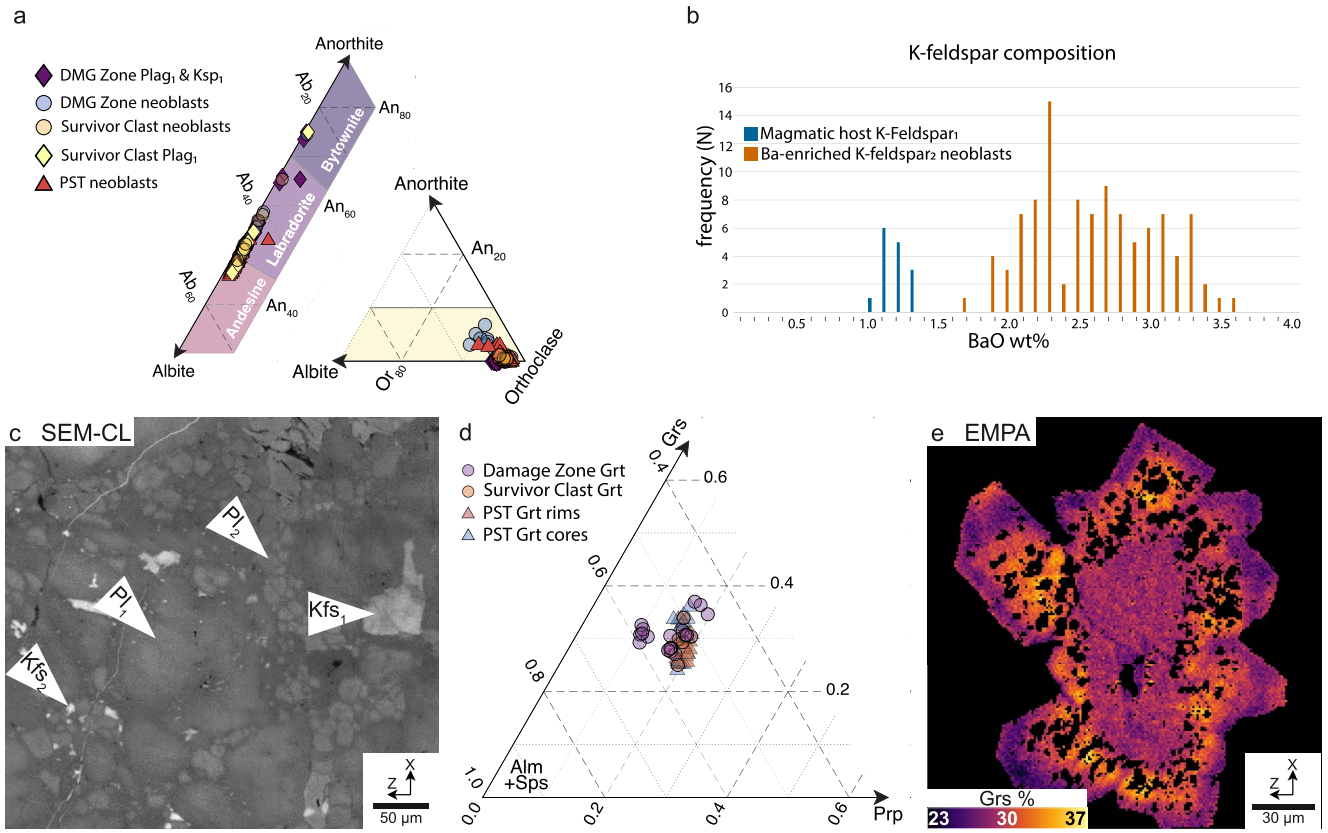

Figure 3. Representative mineral chemistry and microstructures in LM1726 feldspars and garnets. (a) Calculated end-members from all EMP analyses plotted onto the feldspar ternary diagram. (b) Histogram of K-feldspar composition in relation to BaO wt.%. K-feldspar$_1$ contains less BaO than K-feldspar$_2$. (c) SEM-CL of K-feldspar microstructures in the damage zone. K-feldspar$_1$ are large angular fragments (~100 µm size) of intermediate gray CL intensity, while the smaller K-feldspar$_2$ neoblasts are much brighter in CL. (d) Calculated end-members for garnet from all EMP analyses plotted onto the garnet ternary diagram. Garnet shows very little variation in composition regardless of its microstructural location. (e) Representative EMP X-ray map of a zoned framboidal garnet. Grossular content shows an increase in the rim.

Plagioclase is an andesine-labradorite with very little variation in mineral chemistry among all plagioclase grains analyzed (279 point analyses; Figure 3a; Table S1 in Supporting Information S1). The average anorthite (An) content in the damage zone plagioclase$_1$ is An$_{52}$, compared to the average plagioclase$_2$ neoblast in the damage zone that is An$_{52}$. The average plagioclase$_2$ neoblast in the pseudotachylyte vein is An$_{49}$. There is no variation in anorthite content between the wall rock on the two sides separated by the pseudotachylyte vein. There is also no detectable major element chemical zoning that could be correlated with the CL-intensity zonation in plagioclase$_1$. BSE and calibrated X-ray maps however do detect a thin (~5 µm) anorthite enrichment along grain boundaries of both plagioclase$_1$ and plagioclase$_2$ in the damage zone (Figures S2a–S2c in Supporting Information S1).

In the damage zone and within the pseudotachylyte vein, K-feldspar$_2$ neoblasts (Or$_{95}$) have a slight enrichment of BaO (~2–4 wt. %) in comparison to K-feldpsar$_1$ from the anorthosite host rock (Or$_{95}$; 126 point analyses). This difference in BaO content creates a distinct bimodal distribution between K-feldspar$_1$ and K-feldspar$_2$ (Figure 3b). The contrast in mineral chemistry between the two K-feldspars creates a CL-intensity signature in CL maps as the barium-enriched K-feldspar$_2$ grains appear bright white, while K-feldspar$_1$ is a duller white-gray (Figure 3c). In both damage zones flanking either side of the pseudotachylyte vein, K-feldspar$_2$ has a consistent composition. No measurable gradient in BaO content in K-feldspar$_2$ was observed with increasing distance away from the pseudotachylyte vein margin into the damage zone, for the distance sampled in this study (15 mm).

Average garnet chemical composition is Alm$_{41}$ Prp$_{34}$ Sps$_1$ Grs$_{24}$ from a total of 74 point analyses (Figure 3d). Calibrated X-ray maps of both single grain and framboidal garnets in the pseudotachylyte show a diffuse core-to-rim zoning of grossular (Grs$_{37\text{-}23}$; Figure 3e). Small (<25 µm sized) inclusion-free garnets are also present in plagioclase survivor clasts and typically have a composition similar to the inclusion-free rims of pseudotachylyte garnets (Figures S1a and S1e in Supporting Information S1). Compositions of the damage zone garnets, which are also inclusion-free, are similar to the rims of the pseudotachylyte garnets.

4.1.2. Mylonitized Pseudotachylyte

The mylonitized pseudotachylyte (type-1 pseudotachylytes) consists of sheared polymineralic layers derived from the original pseudotachylyte veins alternating with variably deformed and elongated plagioclase-rich lenses representing the deformed lithic clasts of the host anorthosite (Figures 4a and 4b). Domains of either material have varying thicknesses from 10s of μm to 1–2 mm, can be planar or may host small open to tight folds usually verging in the direction of shearing.

The mylonitized pseudotachylyte material consists of a well-mixed matrix of plagioclase, amphibole and clinopyroxene (~5–30 μm), with a subordinate amount of garnet, K-feldspar, quartz, biotite, scapolite, and ilmenite. The matrix amphibole forms isolated grains (~10 μm) or small clusters at the triple junctions between plagioclase grains (Figures 4c and 4d).

Mylonitized pseudotachylytes wrap around plagioclase-rich domains (Figure 4a), as well as ortho- and clinopyroxene grains that are variably replaced by biotite, quartz, amphibole, and garnet aggregates (Figures 4a and 4d). Plagioclase-rich domains are comprised of polycrystalline aggregates of fragmented plagioclase ($plagioclase_1$) and neoblasts of plagioclase ($plagioclase_2$; Figures 4b and 4e). The fragmented $plagioclase_1$ display similar microstructures described earlier in the host anorthosite damage zone (i.e., undulatory extinction, bent deformation twins, and SEM-CL core-to-rim zoning, Figure 4b) and the survivor clasts found within the pristine pseudotachylyte. $Plagioclase_2$ neoblasts are small polygonal grains (<30 μm) with $K\text{-feldspar}_2$ (with bright CL intensity) locally occurring at triple junctions. $K\text{-feldspar}_2$ locally forms 200 μm long by <30 μm wide domains elongate parallel to the foliation and with lobe and cuspate contacts against the surrounding plagioclase (Figure 4c). The cusps are preferentially elongated perpendicular to the foliation. Inclusion-free single and framboidal garnets are scattered infrequently in the monomineralic plagioclase foliations. Garnets are locally surrounded by asymmetrical rims of K-feldspar elongated parallel to the foliation (Figure 4c), similar to the microstructure observed in the pseudotachylyte.

Representative analyses for feldspar and garnet from both monomineralic and polymineralic domains are found in Table S2 of the Supporting Information S1, with accompanying plagioclase and garnet ternary diagrams (Figures S3a and S3b in Supporting Information S1 respectively). These data are consistent with those from Menegon et al. (2017). Plagioclase in the mylonitized pseudotachylyte ranges compositionally from andesine to labradorite as in the pristine pseudotachylyte; however, monomineralic domains are dominantly labradorite (An_{53}), while the polymineralic domains are more andesine (An_{47}; Figure S3a in Supporting Information S1). Also similar to the pristine pseudotachylyte, K-feldspar has a small enrichment in Ba, which again creates a bright CL response (Figure 4c). Garnet has similar core and rim compositions in the mylonitized pseudotachylyte as it does in the pristine pseudotachylyte, and often displays similar diffuse core-to-rim zoning of the grossular component.

4.2. EBSD Analysis of the Mylonitized Pseudotachylyte

EBSD data show that plagioclase in the polymineralic and monomineralic domains of the mylonitized pseudotachylyte show no clear alignment of lattice planes and axes with the foliation nor with the stretching lineation (Figures S4a and S4b in Supporting Information S1). The random pair misorientation angle distribution histogram for both polymineralic and monomineralic domains follows the theoretical curve closely up to angles <60°, and then departs significantly from the curve at higher angles.

4.3. Analysis of Microporosity

An overview of the microporosity is presented in Figure 5, Figures S5 and S6 as well as in Table S3 of the Supporting Information S1 from all eight SμCT volumes analyzed.

4.3.1. Pseudotachylyte Vein and Its Damage Zone

SμCT data reveals porosity is largely concentrated in the pristine pseudotachylyte vein with values ranging between 0.09 and 0.18 vol%, while the damage zone of the host anorthosite contains about 0.01–0.04 vol% porosity (Figure 6a; Table S3a in Supporting Information S1; Movies S1 and S2). A transect through the vein and the flanking damage zone shows a dramatic reduction in porosity between the vein and the damage zone (Figure 6b), from 0.18 vol% to 0.02 vol%. The damage zone immediately along the vein margin contains the least amount of

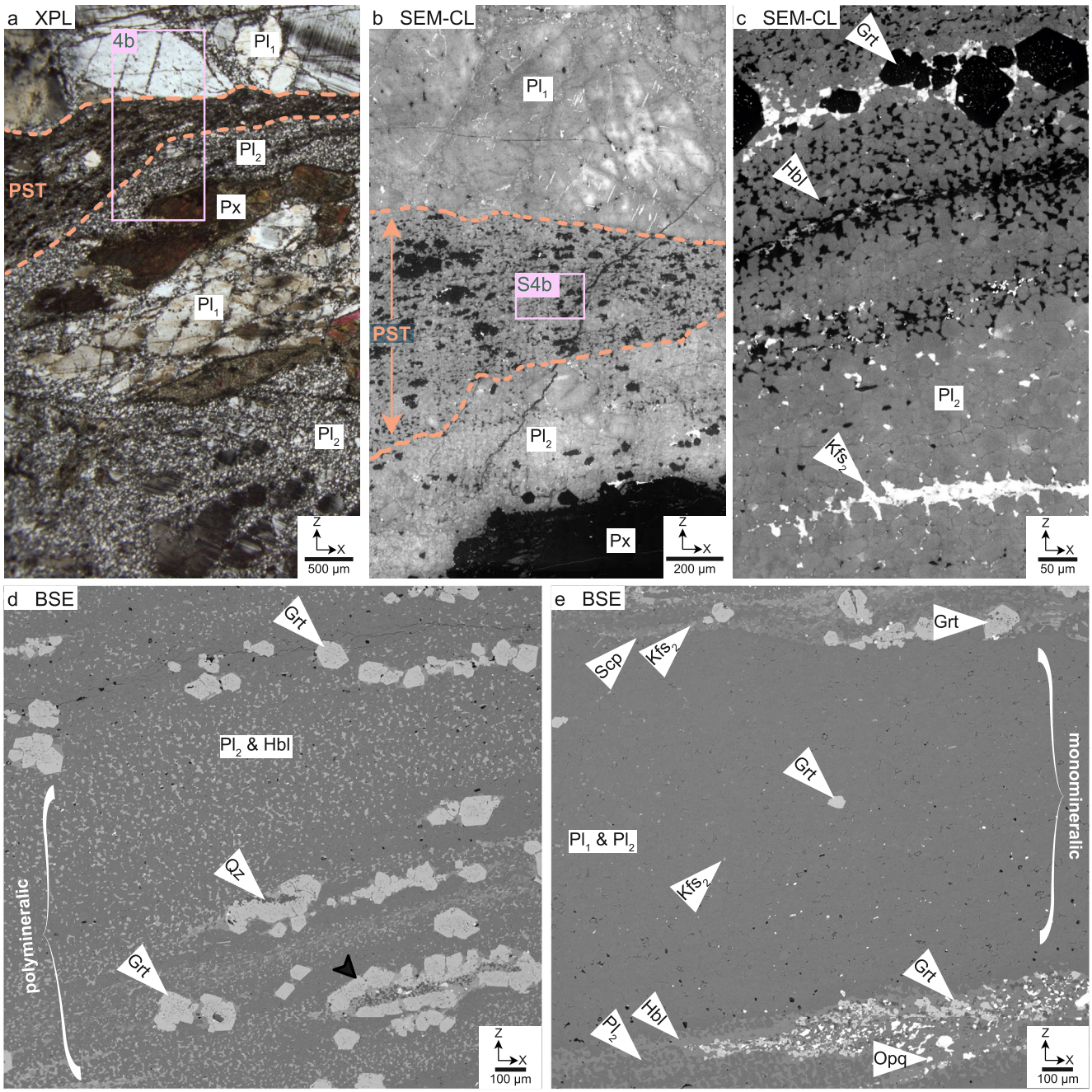

Figure 4. Representative microstructures in mylonitized pseudotachylytes. Shear-sense is top-to-the-right in all images. (a) Sheared pseudotachylyte (PST) vein cross-cutting and wrapping around variably fractured and fragmented plagioclase$_1$ grains that have been variably recrystallized to finer plagioclase$_2$ grains. Cross-polarized light microscopy. (b) SEM-CL of the sheared pseudotachylyte vein in (a). Plagioclase$_1$ displays core-to-rim CL intensity zonation similarly observed in the damage zone and survivor clasts of pristine pseudotachylytes. (c) Sheared pseudotachylyte (polymineralic domain) and sheared survivor clast (~monomineralic domain). Note the cuspate and lobate "teeth" in the bright CL K-feldspar$_2$ ribbon within the monomineralic domain, as well as the well-mixed plagioclase and amphibole polymineralic domain. (d) Backscatter electron (BSE) image of sheared pseudotachylyte matrix (polymineralic domain) that shows a well-mixed foliation containing hornblende and plagioclase$_2$ with a subordinate amount of garnet. Note that some framboidal garnets remain intact, while others have broken up and formed planar aggregates. Garnet often forms coronas around Fe-Ti oxides and pyroxene survivor clasts that are partially replaced by amphibole, quartz, and biotite (black arrow). (e) BSE image of a sheared survivor clast (monomineralic domain) that is largely composed of plagioclase$_1$ and plagioclase$_2$. At the bottom of the image is a polymineralic domain, that is composed of a well-mixed mixture of plagioclase and amphibole on the left side, and on the right side is an aggregate of garnet, Fe-Ti oxides, and pyroxene that is mostly replaced by amphibole and quartz.

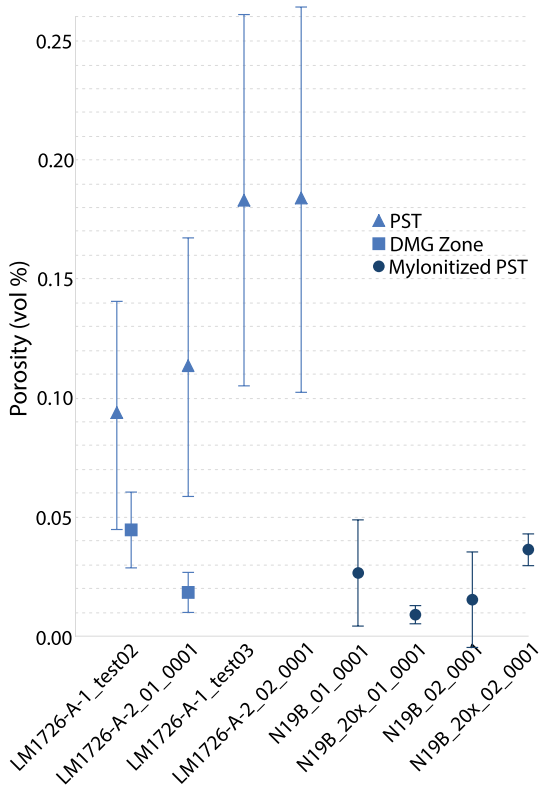

Figure 5. Scatter plot of the calculated porosities from all SμCT volumes. Error bars represent the standard deviation calculated from the binary threshold segmentation of each respective volume. To summarize: the pseudotachylyte vein contains more porosity than the adjacent damage zone, while the mylonitized pseudotachylyte, on average, contains the least amount of porosity.

porosity with 0.01 vol%, and then increases slightly to 0.04 vol% ~500 μm further away from the vein margin. Small (1–10 μm in diameter) isolated pores are found in higher concentration in two specific microdomains: in close proximity to garnet in the pseudotachylyte matrix (within <20 μm of the grain boundary; Figures 6e and 6f), and as inclusions in survivor clasts of the host anorthosite enclosed in the pseudotachylyte (Figure 6g). Pores are also interspersed in the pseudotachylyte matrix amongst the amphibole and plagioclase grains; however, the relationship between pores with garnet is less ambiguous.

Pores in the pseudotachylyte vein have a median volume of ~60–80 μm^3, are bladed to elongated in shape, and occur isolated and disconnected throughout the vein (Figure S7 in Supporting Information S1, Movies S3 and S4). Porosity is concentrated more around garnets (0.25–0.41 vol%; Figure 6e; Figure S17 in Supporting Information S1) than in the surrounding pseudotachylyte matrix (0.07–0.21 vol%; Table S3a in Supporting Information S1). FIB-SEM nanotomography reveals that pores are preferentially found along garnet-plagioclase$_2$, garnet-K-feldspar$_2$ and K-feldspar$_2$-plagioclase$_2$ phase boundaries (Figure 7a; Movie S5). Pores are locally elongated parallel to the elongated rims of K-feldspar$_2$ around garnet. Framboidal garnets host thin interconnected pore networks weaving in and out of the interior chambers of the framboidal clusters (Figure 6f; Movie S6). Both single and framboidal garnet show an asymmetrically distributed rim of pores (Figures 6e and 6f; Figure S8 in Supporting Information S1) and these pores show some amount of interconnectivity as well as a preferred elongation sub-parallel to the instantaneous stretching axis for the weak dextral solid-state shear overprint of the vein (Figure 6c). It is common to find the smallest garnets (<2 μm) in the pseudotachylyte vein in contact with at least one pore.

Plagioclase survivor clasts segmented in SμCT (Figure 6g) show a range (0.44–0.59 vol%) of porosity. Volumetrically smaller clasts have less porosity compared to the larger clasts. Generally, the pores in survivor clasts have a median size ranging 27–64 μm^3 and are somewhat more interconnected than the pores in the pseudotachylyte matrix (Movie S7), but are overall less abundant.

The damage zone in the host anorthosite contains less porosity than the pseudotachylyte vein (Figure 6b). Pores have a median pore volume of ~50–70 μm^3, are often bladed in shape, however they lack an shape-preferred orientation (SPO; Figure 6d and Figure S9 in Supporting Information S1). Where there is porosity, it appears along fracture planes of the fragmented host anorthosite and this porosity can be somewhat interconnected forming relatively large pores (gray arrows in Figure 6a; Figure S10 in Supporting Information S1; Movies S1 and S2). Average pore sizes and maximum pore sizes are typically larger in the damage zone than in the pseudotachylyte; however, total pore count is significantly lower, thus reflecting the overall lower porosity (Table S3a in Supporting Information S1). Porosity is not closely associated with garnets in the damage zone as is seen in the pseudotachylyte vein. A FIB-SEM nanotomography transect along an intracrystalline fracture in a fragmented plagioclase$_1$ grain sealed by K-feldspar$_2$ reveals a near complete lack of porosity (Figure 7b; Movie S8). K-feldspar$_2$ is partially replaced by a vermicular intergrowth of quartz and plagioclase.

4.3.2. Mylonitized Pseudotachylyte

The four mylonitized pseudotachylyte SμCT volumes examined show consistent overall porosity of 0.01–0.04 vol% (Figure 5; Table S3b in Supporting Information S1). The mylonites host significantly less porosity than the pristine pseudotachylyte veins—pores are both smaller (median size: ~32–48 μm^3 for voxel sizes of 0.65^3 μm^3) and, overall, less abundant in the mylonitized pseudotachylyte. Where there is porosity, it is concentrated within monomineralic domains of plagioclase (0.01–0.07 vol%; Figure 8a (black arrow) and Figure 8b; Movies S9 and S10). These domains are interpreted as sheared survivor clasts of the host anorthosite and can contain a minor amount of sporadically scattered single garnet grains. Pores in the monomineralic domains have a median size

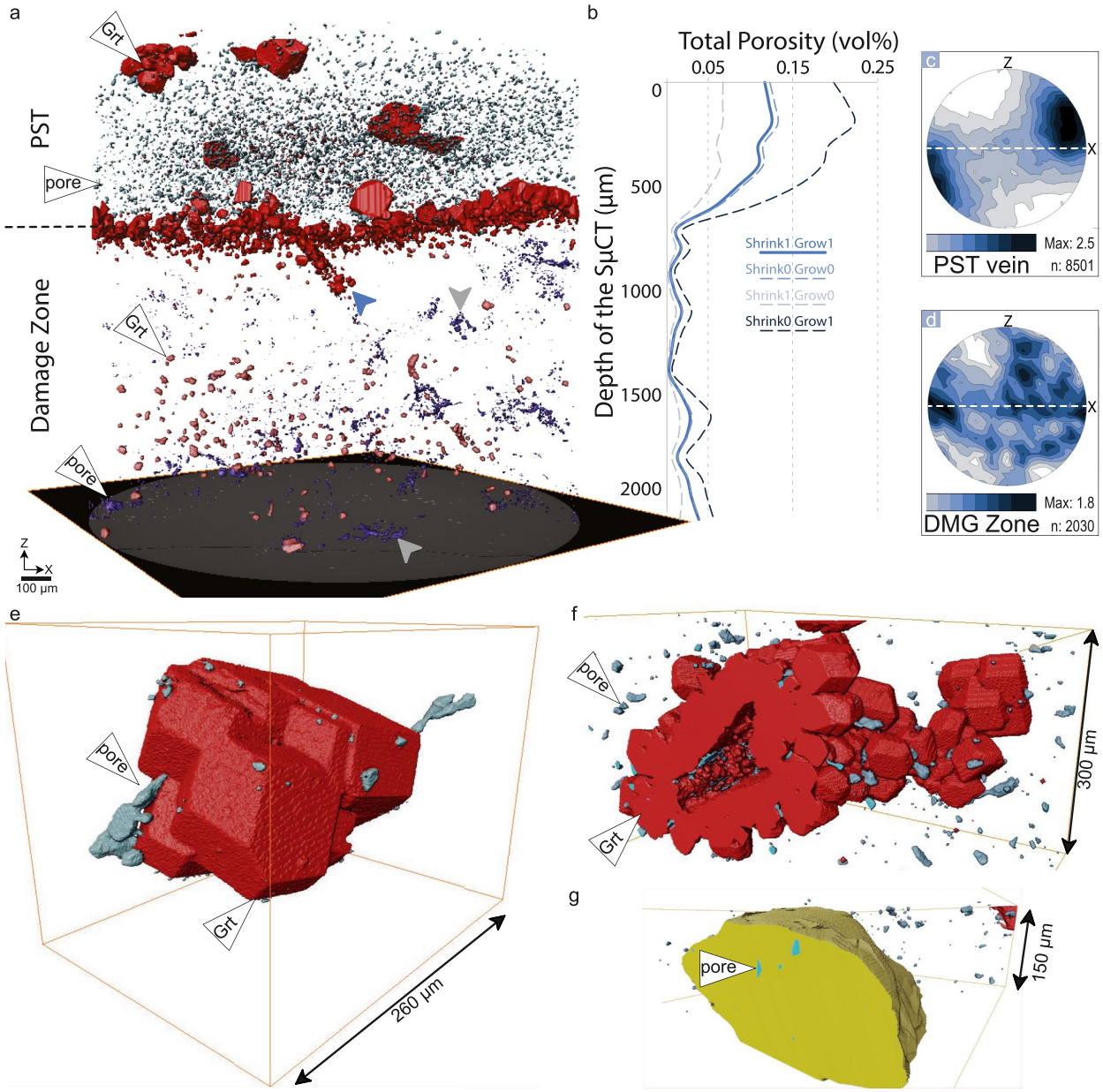

Figure 6. Porosity distribution in the pristine pseudotachylyte. (a) Side-by-side comparison of a representative pristine pseudotachylyte (PST) with damage zone and (b) the porosity distribution as a function to depth extracted from this SμCT volume. Blue arrow in (a) indicates a collection of garnet grains at a high angle to the pseudotachylyte vein margin, which is interpreted as an injection vein. Gray arrows in (a) point to relatively large and interconnected pores in the damage zone. Four lines are plotted in (b) to show the variation of the porosity data depending on the binary thresholding segmentation implemented, however the overall trend remains true in each line. Stereoplots of both the pseudotachylyte vein (c) and the damage zone (d) reveal the orientations of the long axis of individual pores. The pseudotachylyte vein (c) has a strong shape-preferred orientation toward the stretching lineation, while the damage zone pores (d) are randomly orientated. (e) Representative single garnet grain (red) with numerous pores (blue) residing along the grain boundary or in very close proximity. Only pores immediately next to the garnet (<20 μm) are shown. (f) Cross-section view of a representative framboidal garnet with a core consisting of iron or iron-titanium oxides (not segmented) and an interconnected network of thin pores residing within. See Movie S6. (g) Plagioclase survivor clast containing few but relatively large and somewhat interconnected pores.

of ~31 μm^3 (for voxel sizes of 0.65^3 μm^3) are not interconnected, and have a bladed to elongated shape (Figure S11a in Supporting Information S1). The long axes of pores show a rough concentration along a girdle subparallel to the foliation (Figure 8c). Polymineralic foliations consisting of sheared pseudotachylyte matrix material (plagioclase, amphibole and garnet) contain very little porosity (0.01 vol%) with a median pore size of ~18 μm^3 (for voxel sizes of 0.65^3 μm^3). They are bladed to elongated in shape (Figure S12a in Supporting Information S1),

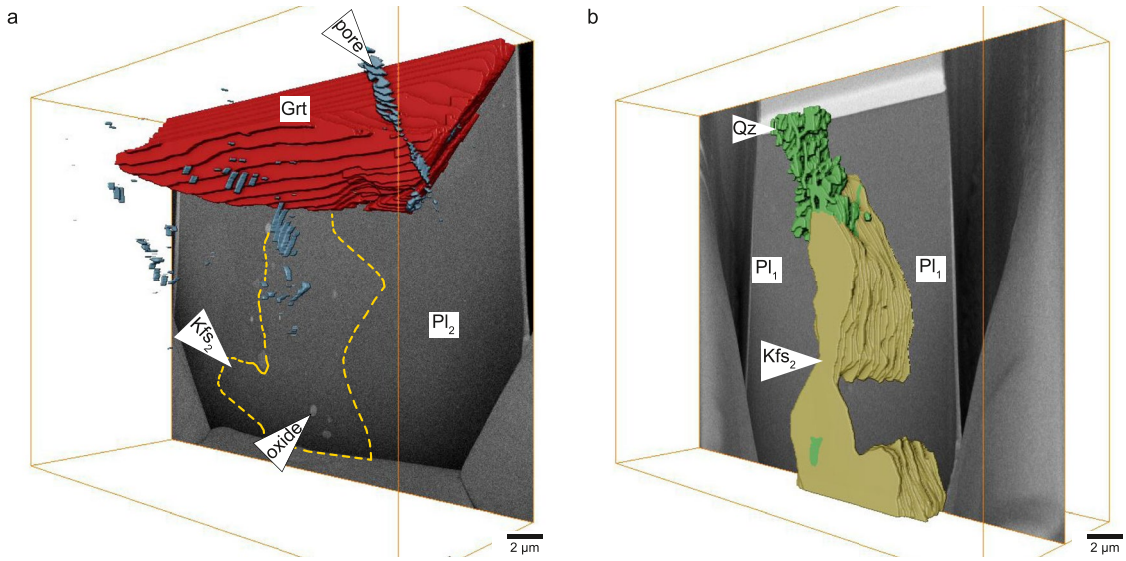

Figure 7. Focused-ion-beam scanning electron microscopy nanotomography segmented volumes with representative microstructures from (a) the pseudotachylyte vein and (b) the damage zone. See Movies S5 and S8 respectively. (a) Garnet grain with associated pores situated along grain and phase boundaries with K-feldspar$_2$ and plagioclase$_2$. Pores are elongated in the incremental extension direction. (b) K-feldspar$_2$ is partially replaced by a vermicular intergrowth of quartz and plagioclase found in a healed fracture within a plagioclase$_1$ grain.

and show a preferred orientation of the long axis nearly parallel to the stretching lineation (Figure 8d). When analyzing a larger data set of pores from an entire SμCT volume (Figure 8e, Figures S13 and S16 in Supporting Information S1), there is a girdle that forms along the foliation of the sheared pseudotachylyte, with a significant population orientated parallel to the stretching lineation.

5. Discussion

5.1. Origin of Porosity at Lower-Crustal Conditions

The microstructures in Figures 6–8 are interpreted to be pores and not vesicles, because at lower-crustal conditions, high lithostatic pressures would render H_2O- and CO_2-bearing fluids (if present in any quantity) completely miscible in the frictional melt (Gomila et al., 2021). At these conditions, it is unlikely that there would be degassing of the melt during crystallization to form vesicles. The Nusfjord lower-crustal anorthosites emplaced at granulite-facies conditions show no macroscopic evidence for fluid infiltration after the development of the pseudotachylytes and mylonites (Menegon et al., 2017). Thus, an origin of porosity in conjunction with exhumation under retrograde metamorphic conditions is unlikely. It is conceivable that some micro- and nanopores related to opening of grain and phase boundaries were created as a decompression-related thermoelastic response to cooling during uplift (Wirth et al., 2022). However, the elongation and shape preferred orientation of the pores associated with garnet in both the pristine- and mylonitized pseudotachylyte (Figures 6c, 6e, 7a, and 8e; Figure S8 in Supporting Information S1) suggests that this porosity is related to processes operating during garnet growth (discussed in Section 5.3) and viscous deformation respectively (Section 5.4). Therefore, we interpret these pores to have formed at lower-crustal depths.

5.2. Preservation of Coseismic Porosity and of Fluid-Rock Interactions in the Damage Zone

The earthquake rupture propagation resulted in a damage zone that transiently hosted a network of well-interconnected fracture porosity, before it was efficiently sealed and healed by solution-precipitation mechanisms, as is commonly seen in the upper crust (e.g., Evans et al., 1997; Kirilova et al., 2020; Mitchell & Faulkner 2012; Figure 9). Remnants of these interconnected pores are found in small clusters (Figure 6a; Figure S10 in Supporting Information S1), and in survivor clasts within the pseudotachylyte (Figure 6g). After the rupture propagation stage, the resulting enhanced permeability contributed to some limited fluid flow, which in turn aided the nearly solid-state recrystallization and the sealing of porosity, thereby effectively healing the

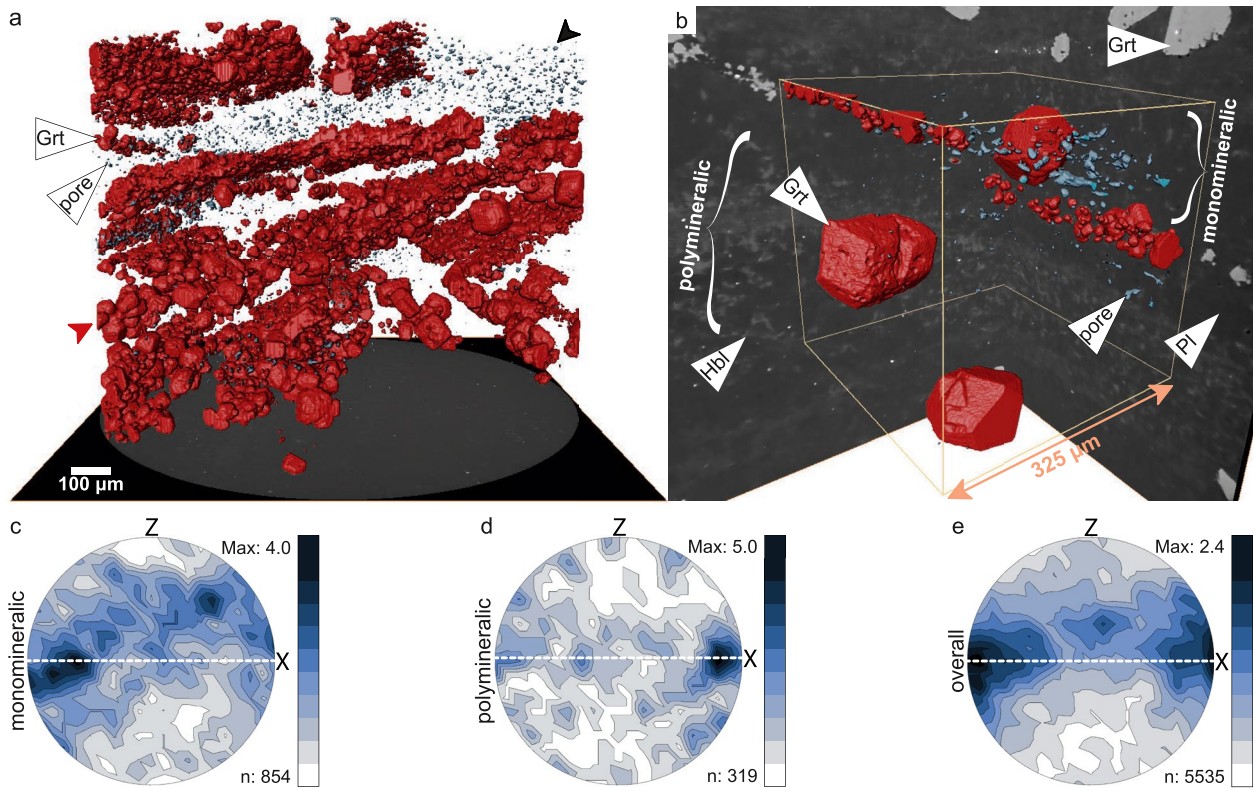

Figure 8. (a) Porosity distribution in the mylonitized pseudotachylyte, with a black arrow indicating the monomineralic domains (sheared survivor clasts) and the red arrow indicating a polymineralic domain (sheared pseudotachylyte matrix). The sheared pseudotachylyte matrix is represented by the segmentation of garnet; however, similar to BSE images in Figures 4d and 4e, these polymineralic domains are aggregates frequently composed of amphibole, plagioclase, garnet, Fe-Ti oxides, along with other minor phases. (b) Segmented subvolume (325^3 µm^3) bounded by YZ and XZ radiographs. The polymineralic domain is a phase mixture dominated by amphibole and plagioclase with two ~100 µm diameter garnets, a few very small pores, and a fine-grained garnet aggregate marking the boundary with the monomineralic domain in the upper portion of the subvolume. Porosity is concentrated in the monomineralic domain, which is composed largely of plagioclase with a single ~100 µm diameter garnet that is surrounded by pores. (c) Pores in monomineralic domains are anisotropic in shape and align to form an shape-preferred orientation orientated subparallel toward the stretching lineation. (d) The polymineralic domains contain much less porosity; however, the pores do align toward the stretching lineation, similar to the monomineralic layer. (e) Orientation of all pores in an entire mylonitized pseudotachylyte SµCT volume.

damage zone. Sealing and healing of the fractures in the damage zone was led primarily by the nucleation of plagioclase$_2$ and K-feldspar$_2$ (Figure 1a; Figure S1c in Supporting Information S1). The lack of micas, the presence of K-feldspar$_2$, and a chemically homogeneous core in both plagioclase$_1$ and plagioclase$_2$, suggests limited fluid availability and limited element transport (Zertani et al., 2022).

The host anorthosite is dominantly composed of plagioclase$_1$, which when comminuted during the rupture, provided the nuclei necessary for neoblasts of plagioclase$_2$ to grow from (e.g., Menegon et al., 2013; Petley-Ragan et al., 2018). The edges (<1 µm) of plagioclase$_1$ and plagioclase$_2$ grain boundaries in the fractures are locally depleted in Na and enriched in Ca (Figures S2a–S2c in Supporting Information S1). These microstructures are similar to the "complex feldspar" or "reversely zoned plagioclase" found elsewhere in lower-crustal anorthosites subjected to fluid infiltration after earthquake faulting, and generally attributed to fracturing followed by fluid-mediated recrystallization (Mukai et al., 2014; Petley-Ragan et al., 2018, 2021; Soda et al., 2020).

K-feldspar$_2$ is finer grained than plagioclase$_2$ and often fills triple junctions and the finest intragranular cracks in the damage zone (Figures 2a, 2c, and 3c). K-feldspar$_2$ neoblasts contain double the amount of BaO than K-feldspar$_1$ (Figure 3b), and K-feldspar$_2$ has the same composition in the damage zone as in the pseudotachylyte vein (Figure 3a). Thus, we conclude that the Ba-enrichment resulted from the coseismic deformation, as there is no sign of a late-stage fluid infiltration during exhumation (Menegon et al., 2017). The questions of the fluid origin and of the likely distance over which aqueous fluid may have moved remain to be addressed. The H_2O content in the anorthosite was on the order of 0.04 wt. % and there was no free H_2O at the *P-T* conditions of deformation (Menegon et al., 2017). The amount of H_2O must have increased by at least 6–10 times to stabilize the

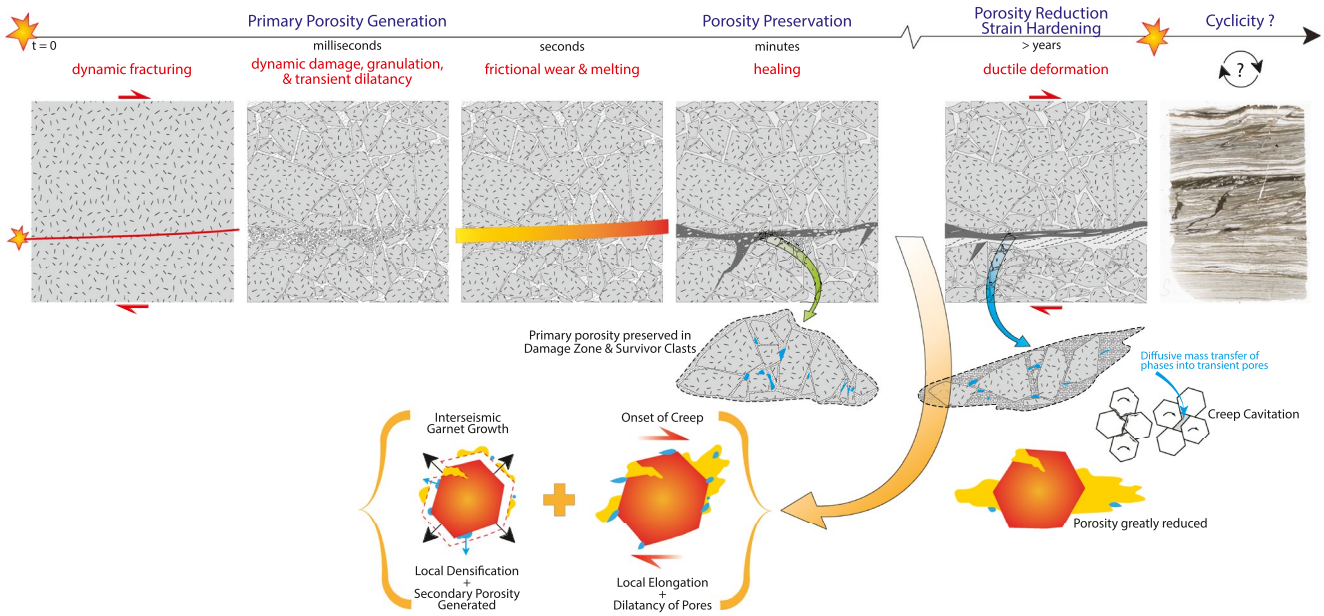

Figure 9. Cartoon summarizing the porosity generating mechanisms in relation to the earthquake cycle and the evolution of a pristine pseudotachylyte into a mylonitized pseudotachylyte. See text for details.

amphibole-bearing assemblage in the mylonitized pseudotachylytes. We speculate that the small amount of biotite (1%–3% modal abundance) in the host anorthosite, and nano-inclusions of Ba-oxides in plagioclase$_1$ (Michalchuk et al., 2023a), provided the Ba for K-feldspar$_2$. This small amount of biotite also provided the 0.25–0.45 wt.% H_2O that migrated along the fracture network in the damage zone, which created the Ca-Na grain-boundary zoning in plagioclase described earlier and transported the K-feldspar$_2$ material in solution. Therefore, we interpret that one source of the H_2O that infiltrated the seismogenic fault is represented by biotite melted during coseismic frictional heating (Figure 9). A limited amount of H_2O was present along the cracks also after the precipitation of K-feldspar$_2$, as indicated by the development of myrmekite, which requires fluid-assisted element transport along grain boundaries (Menegon et al., 2006; Simpson & Wintsch, 1989).

5.3. Origin of Porosity by Densification During Garnet Growth in the Post- and Interseismic Stages

Porosity in the pseudotachylyte veins is preserved because the poor interconnectivity between pores (Figure 6) resulted in an effectively impermeable volume. This is corroborated in Figure 2b where along the pseudotachylyte vein margin with the damage zone, biotite occurs in relatively higher abundance than elsewhere in the pseudotachylyte vein. This suggests that a small amount of fluid was present along the pseudotachylyte boundary, which promoted biotite growth only to a depth of 50–100 μm into the pseudotachylyte vein because the pores were not interconnected.

Garnet with a dendritic to framboidal habit found in pseudotachylyte veins has been interpreted as indicative of nucleation and rapid growth from a frictional melt (Austrheim et al., 1996; Clerc et al., 2018). In our samples, the diffuse core-to-rim zoning of slightly grossular-rich cores to slightly almandine-rich rims (Figure 3e) and the idiomorphic grain shapes, further suggest garnet continued to grow after solidification of the pseudotachylyte melt during the devitrification and recrystallization processes. Reactions in the lower crust can produce phases that are denser than the reactants, and this allows porosity to form, which in itself might represent the pathways for fluids to potentially migrate toward reaction sites (Zertani et al., 2022). We propose that the high concentration of pores in very close proximity to garnets (Figures 6e and 7a; Figure S8 in Supporting Information S1) resulted from a negative volume change reflecting local densification due to garnet growth.

As garnet is denser (3.42–4.31 g/cm^3) than plagioclase (labradorite: 2.68–2.71 g/cm^3) and amphibole (pargasite: 3.07–3.18 g/cm^3), it is worth further investigating how much porosity nearest to the garnet might result from garnet growing at the expense of plagioclase and amphibole. We purposely have not included K-feldspar and biotite

Table 1
Modal Abundances and Mineral Densities Used to Calculate Garnet Densification

	Volume name	LM1726_A1_test02_0001		LM1726_A1_test03		LM1726_A2_01_0001	
	Subvolume name	PST garnet	PST matrix	PST garnet	PST matrix	PST garnet	PST matrix
Modal abundance	Amphibole	0.00%	15.78%	0.00%	13.33%	0.00%	13.94%
	Garnet	98.24%	0.00%	98.13%	0.00%	98.93%	0.00%
	Plagioclase	0.00%	84.22%	0.00%	86.67%	0.00%	86.06%
	Porosity	1.76%	0.00%	1.87%	0.00%	1.07%	0.00%
	Total density (g/cm^3)	3.71	2.74	3.71	2.73	3.74	2.73
	Density difference (g/cm^3) garnet densification	0.97		0.97		1.00	
Densities calculated from Thermolab (g/cm^3)							
Amphibole	3.16						
Garnet	3.78						
Plagioclase	2.67						

in our simplified model because K-feldspar is difficult to segment for with certainty in our SμCT volumes, and biotite is of negligible modal amount. Using microprobe point analyses, we calculated the density differences between a volume containing just garnet and a volume containing plagioclase and amphibole (Grt − (Plag + Amph)) using Thermolab (Vrijmoed & Podladchikov, 2022) at 0.7–0.8 GPa and 650–750°C, following the *P-T* estimates by Menegon et al. (2017). The densities of garnet, plagioclase, and amphibole are near-constant in the investigated *P-T* window (Figure S14 in Supporting Information S1). As a result, the densification due to garnet growth is constant and corresponds to ∼−1.45 g/cm^3. Thus, the local bulk rock in the reaction area becomes denser by 1.45 g/cm^3 as garnet grows and consumes plagioclase and amphibole.

We then followed this by examining if the estimated garnet densification translates to observable porosity in our SμCT data. Using the average densities that were calculated for garnet (3.78 g/cm^3), plagioclase (2.67 g/cm^3), amphibole (3.16 g/cm^3), and porosity (0.00 g/cm^3), we calculated with respect to the modal volume abundance of each phase, the densities of a volume containing just Grt + pores immediately touching garnet, and a volume containing just Pl + Amp (Table 1). The average density difference between the two volumes is 0.98 g/cm^3, which is in range of the 1.45 g/cm^3 calculated above. This translates to 0.35% porosity and is consistent with the porosity measured around the garnets (0.25%–0.41%). Therefore, we conclude that the porosity spatially associated with garnet in the pseudotachylyte vein results from local densification during solid-state garnet growth.

The shape-preferred orientation of elongate pores parallel to the instantaneous stretching axis of the weak solid-state overprint of the pseudotachylyte vein (Figure 6c), suggests that garnet growth and porosity formed during the post- and interseismic stages, when the vein was solidified, and solid-state mineral reactions took place. Asymmetrical rims of K-feldspar$_2$ in strain shadows around garnet also formed during these stages. Development of elongate pores (Figure 7a) in those domains was likely enhanced by the local dilatancy in strain shadows. Thus, while the limited porosity preserved in the damage zone results from coseismic deformation, the isolated pore clusters within the pseudotachylyte vein originated in the post- and interseismic stages by a combination of garnet growth (densification) and weak solid-state overprint (Figure 9). This possibly further promoted limited diffusive mass transfer of ions across reactive areas via the open pores at the garnet grain boundary. Deformation-induced reactions that promoted garnet growth in metastable granites have been linked to the overall densification of the lower crust (Williams et al., 2014).

5.4. Progressive Suppression of Porosity During Interseismic Creep and Conceptual Model of Porosity Evolution During the Earthquake Cycle

Porosity is greatly reduced by over 85% in the mylonitized samples compared to the pristine pseudotachylytes. Polymineralic (pseudotachylyte matrix) and monomineralic (survivor clasts) domains in the mylonitized pseudotachylyte show no crystallographic preferred orientation, fine grain size and polygonal grain shape (Figure S4 in Supporting Information S1). In addition, the polymineralic domains have a high degree of phase mixing, with amphibole (and biotite in minor amounts) found in triple junctions, grain-boundary jogs, and along grain boundaries orientated at large angles to the stretching lineation, suggesting the dominant deformation mechanism was diffusion creep and grain-boundary sliding (Kilian et al., 2011). Menegon et al. (2017) suggested that the plagioclase-rich survivor clasts in their mylonitized pseudotachylyte sample from Nusfjord deformed by dislocation creep, and this would help explain the observation that the rheologically weaker sheared pseudotachylyte material wraps around the stronger survivor clasts. However, the lobate-cuspate K-feldspar microstructures in the plagioclase-dominated survivor clasts (Figure 4c) are textbook examples for diffusion

creep (Gower & Simpson, 1992), as this microstructure is created by the precipitation of material into dilating creep cavities during grain-boundary sliding (Fusseis et al., 2009; Zavada et al., 2007). Thus, we conclude that diffusive mass transfer coupled to grain-boundary sliding (collectively named grain-size sensitive creep, GSS creep) was overall the dominant process in the mylonitized pseudotachylytes from Nusfjord. During GSS creep, pores open and close simultaneously along grain and phase boundaries as grains slide past each other. This forms local transient sites of low stress in which grain-boundary fluids migrate toward and precipitate material—the granular fluid pump model (Fusseis et al., 2009; Kassner & Hayes, 2003; Rybacki et al., 2008, 2010; Zavada et al., 2007). The pore elongation direction is rather scattered, but there is a SPO that has developed subparallel to the stretching lineation (Figure 8e), suggesting that a fraction of pores opened parallel to the elongation direction, similar to what was observed in creep cavitation bands by Menegon et al. (2015). The very little amount of porosity in the polymineralic microdomains (derived from sheared pseudotachylyte matrix) would suggest that the precipitation of intergranular material occurred at a rate that was at least equal to the opening rate (Kilian et al., 2011). In summary, GSS creep operated efficiently at redistributing the material in the transient pores, so that eventually porosity was progressively consumed in the process. This evolution is similar to the strain-depended porosity reduction in eclogites described by Rogowitz and Huet (2021). In our samples, the weakly overprinted pseudotachylyte vein, where diffusive mass transfer was limited, has a remarkably higher porosity than the high-strain, mylonitized pseudotachylyte (Figures 6 and 8), where diffusive mass transfer during interseismic creep was dominant.

With increasing phase precipitation and consumption of grain-boundary fluids, the shear zone became drier. This evolution possibly culminated into shear zone hardening (e.g., Bras et al., 2021; Finch et al., 2016; Rogowitz & Huet, 2021), which may have contributed eventually to the generation of new pseudotachylytes overprinting the mylonites, as frequently observed in Nusfjord (Figure 9; Menegon et al., 2017). Thus, earthquake-induced weakening in the lower crust is transient and occurs only as long as the infiltrated aqueous fluid is available at the grain boundaries. When the fluid is fully consumed, the rocks become strong once more and shear zones may harden and lock (Yardley et al., 2014).

6. Conclusions

Based on the microstructures in pristine and mylonitized pseudotachylytes from Nusfjord, Lofoten, we derived a conceptual model of a dynamically evolving porosity in lower-crustal faults during the earthquake cycle (Figure 9). Coseismic generation of porosity occurred via pulverization-style fragmentation of the wall rock during the dynamic propagation of the earthquake rupture. Fluid-assisted grain growth of feldspar neoblasts within fractures resulted in efficient healing of the wall rock damage. Evidence of fluid infiltration in the damage zone is provided by the enrichment of BaO in K-feldspar$_2$ neoblasts compared to K-feldspar$_1$. Coseismic frictional melting of biotite in the host rock to form pseudotachylytes is interpreted as one source of H_2O and BaO.

The post- and interseismic periods were characterized by the recrystallization of the pseudotachylyte and the onset of solid-state viscous creep. Porosity in the pseudotachylyte is concentrated in imperfectly healed survivor clasts and around garnets, and in minor isolated matrix porosity. Originally framboidal garnets that grew from the quenching frictional melt continued to grow by static recrystallization, exemplified by the core-to-rim zoning pattern. The growth of garnets resulted in the local densification of the volume immediately around the garnet grains, thereby producing the localized increase in porosity. The onset of viscous creep led to a local kinematic control on pore elongation.

Strain localization in the interseismic stage transformed the pseudotachylyte vein into mylonites and was facilitated by grain-size sensitive creep. This resulted in a porosity reduction of >85% in mylonitized pseudotachylytes compared to pristine pseudotachylytes. Diffusive mass transfer and phase precipitation progressively reduced porosity and consumed the grain boundary fluid. This may have led to shear zone hardening, and potentially developed into new generations of pseudotachylytes overprinting the mylonites. Therefore, earthquake-induced rheological weakening of the lower crust is intermittent and occurs only as long as a fluid can infiltrate a transiently permeable shear zone, thereby facilitating diffusive mass transfer.

Data Availability Statement

SμCT and FIB-SEM nanotomography data in the form of .tiff images and the supplementary videos of the segmented volumes can be downloaded from the Norwegian Research Infrastructure Services via https://archive.sigma2.no/welcome.xhtml under a Creative Commons Attribution 4.0 International (CC BY 4.0), using the search "Nusfjord Fault Rocks" published by Michalchuk et al. (2023b).

Acknowledgments
We gratefully thank Melanie Finch and Bruce Yardley for their constructive reviews that improved the manuscript, and Yves Bernabe for editorial handling. Funding for this study was received from the UK Natural Environment Research Council (NERC project "The Geological Record of the Earthquake Cycle in the Lower Crust," Grant NE/P001548/1 to LM) and from the University of Oslo. The Research Council of Norway is acknowledged for support to the Goldschmidt Laboratory national infrastructure (project number 295894). FIB-SEM access was Granted by the European Plate Observing System—Netherlands (www.EPOS-NL.nl). SZ acknowledges funding by the Deutsche Forschungsgemeinschaft (DFG, German Research Foundation; Grant 461241592). This project has received funding from the European Research Council (ERC) under the European Union's Horizon 2020 research and innovation program (Grant 101019628 BREAK to FR), and an ERC starting Grant (Grant 852069 nanoEARTH to OP). Amicia Lee and the SEM staff are thanked for support during the acquisition of the EBSD data at the University of Tromsø.

References

Austrheim, H. (1987). Eclogitization of lower crustal granulites by fluid migration through shear zones. *Earth and Planetary Science Letters*, *81*(2–3), 221–232. https://doi.org/10.1016/0012-821x(87)90158-0

Austrheim, H., Erambert, M., & Boundy, T. M. (1996). Garnets recording deep crustal earthquakes. *Earth and Planetary Science Letters*, *139*(1–2), 223–238. https://doi.org/10.1016/0012-821X(95)00232-2

Berg, S., Kutra, D., Kroeger, T., Straehle, C. N., Kausler, B. X., Haubold, C., et al. (2019). Ilastik: Interactive machine learning for (bio)image analysis. *Nature Methods*, *16*(12), 1226–1232. https://doi.org/10.1038/s41592-019-0582-9

Boullier, A.-M., Ohtani, T., Fujimoto, K., Ito, H., & Dubois, M. (2001). Fluid inclusions in pseudotachylytes from the Nojima fault, Japan. *Journal of Geophysical Research*, *106*(B10), 21965–21977. https://doi.org/10.1029/2000JB000043

Bras, E., Baïsset, M., Yamato, P., & Labrousse, L. (2021). Transient weakening during the granulite to eclogite transformation within hydrous shear zones (Holsnøy, Norway). *Tectonophysics*, *819*, 229026. https://doi.org/10.1016/j.tecto.2021.229026

Campbell, L. R., & Menegon, L. (2022). High stress deformation and short-term thermal pulse preserved in pyroxene microstructures from exhumed lower crustal seismogenic faults (Lofoten, Norway). *Journal of Geophysical Research: Solid Earth*, *127*(7), 25. https://doi.org/10.1029/2021jb023616

Campbell, L. R., Menegon, L., Fagereng, A., & Pennacchioni, G. (2020). Earthquake nucleation in the lower crust by local stress amplification. *Nature Communications*, *11*(1), 1322. https://doi.org/10.1038/s41467-020-15150-x

Clerc, A., Renard, F., Austrheim, H., & Jamtveit, B. (2018). Spatial and size distributions of garnets grown in a pseudotachylyte generated during a lower crust earthquake. *Tectonophysics*, *733*, 159–170. https://doi.org/10.1016/j.tecto.2018.02.014

Copley, A., Avouac, J. P., Hollingsworth, J., & Leprince, S. (2011). The 2001 M-w 7.6 Bhuj earthquake, low fault friction, and the crustal support of plate driving forces in India. *Journal of Geophysical Research: Solid Earth*, *116*(B8), 11. https://doi.org/10.1029/2010jb008137

Corfu, F. (2004). U-pb age, setting and tectonic significance of the anorthosite-mangerite-charnockite-granite suite, Lofoten-Vesteralen, Norway. *Journal of Petrology*, *45*(9), 1799–1819. https://doi.org/10.1093/petrology/egh034

Craig, T. J., Copley, A., & Jackson, J. (2012). Thermal and tectonic consequences of India underthrusting Tibet. *Earth and Planetary Science Letters*, *353*, 231–239. https://doi.org/10.1016/j.epsl.2012.07.010

Craig, T. J., Jackson, J. A., Priestley, K., & McKenzie, D. (2011). Earthquake distribution patterns in Africa: Their relationship to variations in lithospheric and geological structure, and their rheological implications. *Geophysical Journal International*, *185*(1), 403–434. https://doi.org/10.1111/j.1365-246X.2011.04950.x

Dunkel, K. G., Zhong, X., Arnestad, P. F., Valen, L. V., & Jamtveit, B. (2021). High transient stress in the lower crust: Evidence from dry pseudotachylytes in granulites, Lofoten archipelago, northern Norway. *Geology*, *49*(2), 135–139. https://doi.org/10.1130/g48002.1

Evans, J. P., Forster, C. B., & Goddard, J. V. (1997). Permeability of fault-related rocks, and implications for hydraulic structure of fault zones. *Journal of Structural Geology*, *19*(11), 1393–1404. https://doi.org/10.1016/s0191-8141(97)00057-6

Finch, M. A., Weinberg, R. F., & Hunter, N. J. R. (2016). Water loss and the origin of thick ultramylonites. *Geology*, *44*(8), 599–602. https://doi.org/10.1130/G37972.1

Fusseis, F., Regenauer-Lieb, K., Liu, J., Hough, R. M., & De Carlo, F. (2009). Creep cavitation can establish a dynamic granular fluid pump in ductile shear zones. *Nature*, *459*(7249), 974–977. https://doi.org/10.1038/nature08051

Gomila, R., Fondriest, M., Jensen, E., Spagnuolo, E., Masoch, S., Mitchell, T. M., et al. (2021). Frictional melting in hydrothermal fluid-rich faults: Field and experimental evidence from the Bolfin fault zone (Chile). *Geochemistry, Geophysics, Geosystems*, *22*(7), 17. https://doi.org/10.1029/2021gc009743

Gower, R. J. W., & Simpson, C. (1992). Phase-boundary mobility in naturally deformed, high-grade quartzofeldspathic rocks—Evidence for diffusional creep. *Journal of Structural Geology*, *14*(3), 301–313. https://doi.org/10.1016/0191-8141(92)90088-e

Hawemann, F., Mancktelow, N. S., Wex, S., Camacho, A., & Pennacchioni, G. (2018). Pseudotachylyte as field evidence for lower-crustal earthquakes during the intracontinental Petermann Orogeny (Musgrave Block, Central Australia). *Solid Earth*, *9*(3), 629–648. https://doi.org/10.5194/se-9-629-2018

Jackson, J. A., Austrheim, H., McKenzie, D., & Priestley, K. (2004). Metastability, mechanical strength, and the support of mountain belts. *Geology*, *32*(7), 625. https://doi.org/10.1130/g20397.1

Jamtveit, B., Austrheim, H., & Putnis, A. (2016). Disequilibrium metamorphism of stressed lithosphere. *Earth-Science Reviews*, *154*, 1–13. https://doi.org/10.1016/j.earscirev.2015.12.002

Jamtveit, B., Petley-Ragan, A., Incel, S., Dunkel, K. G., Aupart, C., Austrheim, H., et al. (2019). The effects of earthquakes and fluids on the metamorphism of the lower continental crust. *Journal of Geophysical Research: Solid Earth*, *124*(8), 7725–7755. https://doi.org/10.1029/2018jb016461

Jolivet, L., Raimbourg, H., Labrousse, L., Avigad, D., Leroy, Y., Austrheim, H., & Andersen, T. B. (2005). Softening trigerred by eclogitization, the first step toward exhumation during continental subduction. *Earth and Planetary Science Letters*, *237*(3–4), 532–547. https://doi.org/10.1016/j.epsl.2005.06.047

Kaatz, L., Zertani, S., Moulas, E., John, T., Labrousse, L., Schmalholz, S. M., & Andersen, T. B. (2021). Widening of hydrous shear zones during incipient eclogitization of metastable dry and rigid lower crust-Holsnoy, western Norway. *Tectonics*, *40*(3), 19. https://doi.org/10.1029/2020tc006572

Kassner, M. E., & Hayes, T. A. (2003). Creep cavitation in metals. *International Journal of Plasticity*, *19*(10), 1715–1748. https://doi.org/10.1016/s0749-6419(02)00111-0

Kilian, R., Heilbronner, R., & Stunitz, H. (2011). Quartz grain size reduction in a granitoid rock and the transition from dislocation to diffusion creep. *Journal of Structural Geology*, *33*(8), 1265–1284. https://doi.org/10.1016/j.jsg.2011.05.004

Kirilova, M., Toy, V., Sauer, K., Renard, F., Gessner, K., Wirth, R., et al. (2020). Micro- and nano-porosity of the active alpine fault zone, New Zealand. *Solid Earth*, *11*(6), 2425–2438. https://doi.org/10.5194/se-11-2425-2020

Kullerud, K., Flaat, K., & Davidsen, B. (2001). High-pressure fluid-rock reactions involving cl-bearing fluids in lower-crustal ductile shear zones of the Flakstadoy Basic Complex, Lofoten, Norway. *Journal of Petrology*, *42*(7), 1349–1372. https://doi.org/10.1093/petrology/42.7.1349

Lanari, P., Vho, A., Bovay, T., Airaghi, L., & Centrella, S. (2019). Quantitative compositional mapping of mineral phases by electron probe micro-analyser. *Geological Society, London, Special Publications*, *478*(1), 39–63. https://doi.org/10.1144/sp478.4

Lanari, P., Vidal, O., De Andrade, V., Dubacq, B., Lewin, E., Grosch, E. G., & Schwartz, S. (2014). XMapTools: A MATLAB©-based program for electron microprobe X-ray image processing and geothermobarometry. *Computers and Geosciences*, *62*, 227–240. https://doi.org/10.1016/j.cageo.2013.08.010

Magloughlin, J. F. (2011). Bubble collapse structure: A microstructural record of fluids, bubble formation and collapse, and mineralization in pseudotachylyte. *The Journal of Geology*, *119*(4), 351–371. https://doi.org/10.1086/659143

Mancktelow, N. S., Camacho, A., & Pennacchioni, G. (2022). Time-lapse record of an earthquake in the dry felsic lower continental crust preserved in a pseudotachylyte-bearing fault. *Journal of Geophysical Research: Solid Earth*, *127*(4), 32. https://doi.org/10.1029/2021jb022878

Markl, G., Frost, B. R., & Bucher, K. (1998). The origin of anorthosites and related rocks from the Lofoten islands, northern Norway: I. Field relations and estimation of intrinsic variables. *Journal of Petrology*, *39*(8), 1425–1452. https://doi.org/10.1093/petroj/39.8.1425

Marone, F., Studer, A., Billich, H., Sala, L., & Stampanoni, M. (2017). Towards on-the-fly data post-processing for real-time tomographic imaging at tomcat. *Advanced Structural and Chemical Imaging*, *3*, 1. https://doi.org/10.1186/s40679-016-0035-9

McBeck, J. A., Cordonnier, B., & Renard, F. (2021). The influence of spatial resolution and noise on fracture network properties calculated from X-ray microtomography data. *International Journal of Rock Mechanics and Mining Sciences*, *147*, 104922. https://doi.org/10.1016/j.ijrmms.2021.104922

Menegon, L., Fusseis, F., Stünitz, H., & Xiao, X. (2015). Creep cavitation bands control porosity and fluid flow in lower crustal shear zones. *Geology*, *43*(3), 227–230. https://doi.org/10.1130/g36307.1

Menegon, L., Pennacchioni, G., Malaspina, N., Harris, K., & Wood, E. (2017). Earthquakes as precursors of ductile shear zones in the dry and strong lower crust. *Geochemistry, Geophysics, Geosystems*, *18*(12), 4356–4374. https://doi.org/10.1002/2017gc007189

Menegon, L., Pennacchioni, G., & Stunitz, H. (2006). Nucleation and growth of myrmekite during ductile shear deformation in metagranites. *Journal of Metamorphic Geology*, *24*(7), 553–568. https://doi.org/10.1111/j.1525-1314.2006.00654.x

Menegon, L., Stünitz, H., Nasipuri, P., Heilbronner, R., & Svahnberg, H. (2013). Transition from fracturing to viscous flow in granulite facies perthitic feldspar (Lofoten, Norway). *Journal of Structural Geology*, *48*, 95–112. https://doi.org/10.1016/j.jsg.2012.12.004

Michalchuk, S. P., Dunkel, K., Ohl, O., & Menegon, L. (2023a). Deformation and healing processes in the damage zone of a lower-crustal seismogenic fault. In *EGU general assembly 2023, EGU23-3414*, Vienna, Austria, 24–28 April 2023. Retrieved from https://meetingorganizer.copernicus.org/EGU23/EGU23-3414.html

Michalchuk, S. P., Menegon, L., Zertani, S., Fusseis, F., Chogani, A., & Plümper, O. (2023b). Nusfjord fault rocks [Dataset]. Norstore. https://doi.org/10.11582/2023.00020

Mitchell, T. M., & Faulkner, D. R. (2012). Towards quantifying the matrix permeability of fault damage zones in low porosity rocks. *Earth and Planetary Science Letters*, *339*, 24–31. https://doi.org/10.1016/j.epsl.2012.05.014

Mukai, H., Austrheim, H., Putnis, C. V., & Putnis, A. (2014). Textural evolution of plagioclase feldspar across a shear zone: Implications for deformation mechanism and rock strength. *Journal of Petrology*, *55*(8), 1457–1477. https://doi.org/10.1093/petrology/egu030

Orlandini, O. F., & Mahan, K. H. (2020). Rheological evolution of a pseudotachylyte-bearing deep crustal shear zone in the western Canadian shield. *Journal of Structural Geology*, *141*, 104188. https://doi.org/10.1016/j.jsg.2020.104188

Petley-Ragan, A., Ben-Zion, Y., Austrheim, H., Ildefonse, B., Renard, F., & Jamtveit, B. (2019). Dynamic earthquake rupture in the lower crust. *Science Advances*, *5*, 7. https://doi.org/10.1126/sciadv.aaw0913

Petley-Ragan, A., Dunkel, K. G., Austrheim, H., Ildefonse, B., & Jamtveit, B. (2018). Microstructural records of earthquakes in the lower crust and associated fluid-driven metamorphism in plagioclase-rich granulites. *Journal of Geophysical Research: Solid Earth*, *123*(5), 3729–3746. https://doi.org/10.1029/2017jb015348

Petley-Ragan, A. J., Plümper, O., Ildefonse, B., & Jamtveit, B. (2021). Nanoscale earthquake records preserved in plagioclase microfractures from the lower continental crust. *Solid Earth*, *12*(4), 959–969. https://doi.org/10.5194/se-12-959-2021

Putnis, A., Jamtveit, B., & Austrheim, H. (2017). Metamorphic processes and seismicity: The Bergen arcs as a natural laboratory. *Journal of Petrology*, *58*(10), 1871–1897. https://doi.org/10.1093/petrology/egx076

Rogowitz, A., & Huet, B. (2021). Evolution of fluid pathways during eclogitization and their impact on formation and deformation of eclogite: A microstructural and petrological investigation at the type locality (Koralpe, Eastern Alps, Austria). *Tectonophysics*, *819*, 19. https://doi.org/10.1016/j.tecto.2021.229079

Rowe, C. D., Moore, J. C., Meneghini, F., & McKeirnan, A. W. (2005). Large-scale pseudotachylytes and fluidized cataclasites from an ancient subduction thrust fault. *Geology*, *33*(12), 937–940. https://doi.org/10.1130/g21856.1

Rybacki, E., Wirth, R., & Dresen, G. (2008). High-strain creep of feldspar rocks: Implications for cavitation and ductile failure in the lower crust. *Geophysical Research Letters*, *35*(4), 5. https://doi.org/10.1029/2007gl032478

Rybacki, E., Wirth, R., & Dresen, G. (2010). Superplasticity and ductile fracture of synthetic feldspar deformed to large strain. *Journal of Geophysical Research: Solid Earth*, *115*(B8), 14. https://doi.org/10.1029/2009jb007203

Simpson, C., & Wintsch, R. P. (1989). Evidence for deformation-induced k-feldspar replacement by myrmekite. *Journal of Metamorphic Geology*, *7*(2), 261–275. https://doi.org/10.1111/j.1525-1314.1989.tb00588.x

Soda, Y., Matsuda, T., Kobayashi, S., Ito, M., Harigane, Y., & Okudaira, T. (2020). Reversely zoned plagioclase in lower crustal meta-anorthosites: An indicator of multistage fracturing and metamorphism in the lower crust. *American Mineralogist*, *105*(7), 1002–1013. https://doi.org/10.2138/am-2020-7284

Steltenpohl, M. G., Hames, W. E., & Andresen, A. (2004). The Silurian to Permian history of a metamorphic core complex in Lofoten, northern Scandinavian Caledonides. *Tectonics*, *23*(1). https://doi.org/10.1029/2003tc001522

Steltenpohl, M. G., Kassos, G., & Andresen, A. (2006). Retrograded eclogite-facies pseudotachylytes as deep-crustal paleoseismic faults within continental basement of Lofoten, North Norway. *Geosphere*, *2*(1), 61. https://doi.org/10.1130/ges00035.1

Steltenpohl, M. G., Kassos, G., Andresen, A., Rehnström, E. F., & Hames, W. E. (2011). Eclogitization and exhumation of Caledonian continental basement in Lofoten, North Norway. *Geosphere*, *7*(1), 202–218. https://doi.org/10.1130/ges00573.1

Thompson, A. B., & Connolly, J. A. D. (1990). Metamorphic fluids and anomalous porosities in the lower crust. *Tectonophysics*, *182*(1–2), 47–55. https://doi.org/10.1016/0040-1951(90)90341-5

Vrijmoed, J. C., & Podladchikov, Y. Y. (2022). Thermolab: A thermodynamics laboratory for nonlinear transport processes in open systems. *Geochemistry, Geophysics, Geosystems*, *23*(4), 44. https://doi.org/10.1029/2021gc010303

Walters, J. B. (2022). Minplot: A mineral formula recalculation and plotting program for electron probe microanalysis. *Mineralogia*, *53*(1), 51–66. https://doi.org/10.2478/mipo-2022-0005

Whitney, D. L., & Evans, B. W. (2010). Abbreviations for names of rock-forming minerals. *American Mineralogist*, *95*(1), 185–187. https://doi.org/10.2138/am.2010.3371

Williams, M. L., Dumond, G., Mahan, K., Regan, S., & Holland, M. (2014). Garnet-forming reactions in felsic orthogneiss: Implications for densification and strengthening of the lower continental crust. *Earth and Planetary Science Letters*, *405*, 207–219. https://doi.org/10.1016/j.epsl.2014.08.030

Wirth, R., Kruhl, J. H., Morales, L. F. G., & Schreiber, A. (2022). Partially open grain and phase boundaries as fluid pathways in metamorphic and magmatic rocks. *Journal of Metamorphic Geology*, *40*(1), 67–85. https://doi.org/10.1111/jmg.12610

Yardley, B. W. D., Rhede, D., & Heinrich, W. (2014). Rates of retrograde metamorphism and their implications for the rheology of the crust: An experimental study. *Journal of Petrology*, *55*(3), 623–641. https://doi.org/10.1093/petrology/egu001

Yardley, B. W. D., & Valley, J. W. (1997). The petrologic case for a dry lower crust. *Journal of Geophysical Research B: Solid Earth*, *102*(B6), 12173–12185. https://doi.org/10.1029/97jb00508

Zavada, P., Schulmann, K., Konopasek, J., Ulrich, S., & Lexa, O. (2007). Extreme ductility of feldspar aggregates—Melt-enhanced grain boundary sliding and creep failure: Rheological implications for felsic lower crust. *Journal of Geophysical Research: Solid Earth*, *112*(B10), 15. https://doi.org/10.1029/2006jb004820

Zertani, S., John, T., Brachmann, C., Vrijmoed, J. C., & Plumper, O. (2022). Reactive fluid flow guided by grain-scale equilibrium reactions during eclogitization of dry crustal rocks. *Contributions to Mineralogy and Petrology*, *177*(6), 18. https://doi.org/10.1007/s00410-022-01928-3

Zertani, S., Labrousse, L., John, T., Andersen, T. B., & Tilmann, F. (2019). The interplay of eclogitization and deformation during deep burial of the lower continental crust-a case study from the Bergen arcs (western Norway). *Tectonics*, *38*(3), 898–915. https://doi.org/10.1029/2018tc005297

References From the Supporting Information

Allmendinger, R. W., Cardozo, N., & Fisher, D. M. (2011). *Structural geology algorithms: Vectors and tensors*. Cambridge University Press.

Angelidakis, V., Nadimi, S., & Utili, S. (2022). Elongation, flatness and compactness indices to characterise particle form. *Powder Technology*, *396*, 689–695. https://doi.org/10.1016/j.powtec.2021.11.027

Buades, A., Coll, B., & Morel, J. M. (2005). A non-local algorithm for image denoising. In *2005 IEEE computer society conference on computer vision and pattern recognition (CVPR'05)* (pp. 20–25). https://doi.org/10.1109/CVPR.2005.38

Gilgannon, J., Fusseis, F., Menegon, L., Regenauer-Lieb, K., & Buckman, J. (2017). Hierarchical creep cavity formation in an ultramylonite and implications for phase mixing. *Solid Earth*, *8*(6), 1193–1209. https://doi.org/10.5194/se-8-1193-2017

Green, E. C. R., White, R. W., Diener, J. F. A., Powell, R., Holland, T. J. B., & Palin, R. M. (2016). Activity–composition relations for the calculation of partial melting equilibria in metabasic rocks. *Journal of Metamorphic Geology*, *34*(9), 845–869. https://doi.org/10.1111/jmg.12211

Holland, T., & Powell, R. (2003). Activity–composition relations for phases in petrological calculations: An asymmetric multicomponent formulation. *Contributions to Mineralogy and Petrology*, *145*(4), 492–501. https://doi.org/10.1007/s00410-003-0464-z

Holland, T. J. B., & Powell, R. (2011). An improved and extended internally consistent thermodynamic dataset for phases of petrological interest, involving a new equation of state for solids. *Journal of Metamorphic Geology*, *29*(3), 333–383. https://doi.org/10.1111/j.1525-1314.2010.00923.x

White, R. W., Powell, R., & Holland, T. J. B. (2007). Progress relating to calculation of partial melting equilibria for metapelites. *Journal of Metamorphic Geology*, *25*(5), 511–527. https://doi.org/10.1111/j.1525-1314.2007.00711.x

Zingg, T. (1935). *Beitrag zur schotteranalyse*. ETH Zurich.